



저작자표시-비영리-변경금지 2.0 대한민국

이용자는 아래의 조건을 따르는 경우에 한하여 자유롭게

- 이 저작물을 복제, 배포, 전송, 전시, 공연 및 방송할 수 있습니다.

다음과 같은 조건을 따라야 합니다:



저작자표시. 귀하는 원저작자를 표시하여야 합니다.



비영리. 귀하는 이 저작물을 영리 목적으로 이용할 수 없습니다.



변경금지. 귀하는 이 저작물을 개작, 변형 또는 가공할 수 없습니다.

- 귀하는, 이 저작물의 재이용이나 배포의 경우, 이 저작물에 적용된 이용허락조건을 명확하게 나타내어야 합니다.
- 저작권자로부터 별도의 허가를 받으면 이러한 조건들은 적용되지 않습니다.

저작권법에 따른 이용자의 권리는 위의 내용에 의하여 영향을 받지 않습니다.

이것은 [이용허락규약\(Legal Code\)](#)을 이해하기 쉽게 요약한 것입니다.

[Disclaimer](#)

이학박사학위논문

**Global warming, low-frequency variability, and biennial
oscillation contribution to the Pacific climate variability
and its decadal changes around the late-1990s**

**태평양 기후의 온난화, 장 주기, 2 년 주기 변동 성분과
1990 년대 후반에 나타난 10 년 변화의 특징**

2013 년 8 월

**서울대학교 대학원
지구환경과학부
여 새 림**

**Global warming, low-frequency variability, and biennial
oscillation contribution to the Pacific climate variability
and its decadal changes around the late-1990s**

**태평양기후의 온난화, 장 주기, 2 년 주기 변동 성분과
1990 년대 후반에 나타난 10 년 변화의 특징**

지도교수 Kwang-Yul Kim

이 논문을 이학박사 학위 논문으로 제출함
2013 년 6 월

서울대학교 대학원
지구환경과학부
여 새 림

여새림의 이학박사 학위논문을 인준함
2013 년 8 월

위 원 장 _____ (인)

부위원장 _____ (인)

위 원 _____ (인)

위 원 _____ (인)

위 원 _____ (인)

Abstract

Global warming, low-frequency variability, and biennial oscillation contribution to the Pacific climate variability and its decadal changes around the late-1990s

Sae-Rim Yeo

School of Earth and Environmental Sciences

The Graduate School

Seoul National University

In order to understand the climate variability over the Pacific, the Pacific climate variabilities are decomposed into distinctive physical modes using a statistical method called cyclostationary empirical orthogonal function (CSEOF) analysis. In the first part of the thesis, three primary global modes of sea surface temperature (SST) variability during the period of 1871-2010 are identified, that is, the global warming mode, the low-frequency variability mode, and the biennial oscillation mode. The three-mode reconstruction captures a significant portion of the observed El Niño-Southern Oscillation (ENSO) variability. In other words, the bulk of ENSO variability is adequately explained in terms of interplay among the three modes. In particular, two key points are derived from this analysis: (1) the

most extreme El Niño events occurred in 1982/83 and 1997/98 are attributed to the positive contributions of all three modes; and (2) the central Pacific (CP) El Niño events in the 1990s and 2000s have different physical mechanisms, that is, the CP El Niño events in the early 1990s originated mainly from the low-frequency mode, while those in the early 2000s derived mainly from the global warming mode.

Meanwhile, the most recent phase transition in the low-frequency variability mode is occurred in 1998/99 from positive to negative phase. In accordance with this phase transition, it is found that the relationship between the tropical Pacific and the North Pacific appears to have significantly changed since 1999. In the second part of the thesis, the characteristics of the connection between the tropical Pacific and the North Pacific during two sub-periods (1980-1998 and 1999-2010) are examined. It is found that the atmospheric anomalies induced by the ENSO alter the SST over the North Pacific through surface heat flux change during the earlier period of 1980-1998. During the later period, in contrast, ENSO-related atmospheric anomalies feature the North Pacific oscillation (NPO) pattern during winter, which is characterized by a southward shift of the atmospheric center of action from its climatological position. The NPO-related atmospheric anomalies extend to the subtropical Pacific; this

extension potentially links midlatitude and tropical Pacific variability through air-sea interactions. The physical change appears to alter the El Niño characteristics into that of the CP El Niño through the wind-SST coupling mechanism.

After 1999, it is obvious that the intensified global warming signal as well as the phase transition in the low-frequency variability. In the third part of the thesis, therefore, it is investigated how the warming signal affects Pacific climate variability. In particular, the relationship between the warming in the sub-arctic Pacific (Bering and Chukchi Seas) and the Pacific climate variability is examined. Specifically, warming in the Bering and Chukchi Seas in the period of 1999-2010 involves sea ice reduction and stronger oceanic heat flux to the atmosphere in winter. The atmospheric response to the recent warming in the Bering and Chukchi Seas resembles the NPO pattern. Further analysis reveals that the recent climate variability in the Bering and Chukchi Seas has strong covariability with large-scale climate modes in the Pacific, that is North Pacific Gyre Oscillation (NPGO) and the CP El Niño.

Keywords

El Niño-Southern Oscillation, Global warming, Cyclostationary EOF

Student number : 2009-20372

Contents

Abstract	i
Table of contents	iv
List of figures	vi
Chapter1. Introduction	1
1.1. Background	1
1.2. Objectives of the thesis	7
Chapter2. Data and methodology	11
2.1. Data	11
2.2. Methodology	12
Chapter3. Global warming, low-frequency variability, and biennial oscillation	16
3.1. Three fundamental modes of SST variability	17
3.2. Characterization of recent ENSO events identified by three CSEOF modes	39
Chapter4. Decadal changes in the relationship between the tropical Pacific and the North Pacific around late-1990s	53
4.1. CSEOF modes of the SSTA over the tropical Pacific and the North Pacific	53
4.2. Changes in the relationship between the tropical Pacific and the North Pacific	60
Chapter5. Relationship between the climate variability in the Bering Sea and large-scale circulation in the Pacific during 1999-2010	85
5.1. Recent warming in the Bering Sea and its relationship to the North Pacific Oscillation	86
5.2. Covariability of Bering Sea and Pacific large-scale circulation	112

Chapter6. Summary and conclusions	118
References	124
국문 초록	134

List of figures

- Fig.3.1.** (a) The loading vector (0° – 360° E, 70° S– 70° N), (b) the corresponding PC (principal component) time series, and (c) the longitude-time cross section averaged over the equatorial region (5° S– 5° N) for the first CSEOF (cyclostationary empirical orthogonal function) mode of SST (sea surface temperature) anomalies. This mode represents global warming/cooling. 20
- Fig.3.2.** The data presented are similar to the data in Fig. 3.1 but are for the second CSEOF mode. The dashed line in (b) represents the 5-year low-pass filtered Nino3 index after removing a linear trend. This mode represents low-frequency SST variability in the Pacific. 24
- Fig.3.3.** The data presented are similar to the data in Fig. 3.1 but are for the third CSEOF mode. This mode represents primarily the biennial oscillations (tendency) of SST in the tropical Pacific. 28
- Fig.3.4.** Lead-lag correlation among the first three CSEOF PC time series 32
- Fig.3.5.** Longitude-time cross section of SSTA (SST anomalies) averaged over the equatorial region (5° S– 5° N) of (a) the raw data, and (b) the reconstructed data based on the first three modes. (c) Nino3 and (d) Nino4 indices obtained from the raw SSTA data (black line) and the 3-mode SSTA reconstruction (orange line). 33
- Fig.3.6.** The (a) first, (b) second, and (c) third CSEOF loading vectors of SSTA and the map of regressed precipitation anomalies corresponding to the (e) first, (f) second, and (g) third CSEOF modes of the SSTA. The SSTA and precipitation differences between the third and second CSEOF modes (mode 3 – mode 2) are presented in (d) and (h), respectively. The presented patterns represent averages from December to February. The CSEOF and regression patterns are scaled by the standard deviation of the respective PC time series (eigenvalues) so that the PC time series have a unit variance. 37

Fig.3.7. The map of regressed air temperature (shade) and geopotential height anomalies (contour) at 1000-hPa (left column), and the map of stream function (contour) and geopotential height anomalies (shade) at 200-hPa (right column) for the first (a and e), second (b and f), and third (c and g) CSEOF modes of SSTA, respectively. The difference between the third and second CSEOF modes (mode 3 – mode 2) are presented in (d) for 1000 hPa air temperature and geopotential height, and (h) for 200 hPa geopotential height and wind. The presented patterns represent averages from December (year 1) to February (year 2). The CSEOF and regression patterns are scaled by the standard deviation of the respective PC time series (eigenvalues) so that the PC time series have a unit variance. 38

Fig.3.8. Longitude-time cross section of the reconstructed SSTA based on the (a) first, (b) second, and (c) third CSEOF modes. (d) The Nino3 (black line) and Nino4 (blue line) indices of the raw SSTA data. The horizontal lines from top to bottom denote 1998/99, 1976/77, and 1959/60 boundaries, respectively. 41

Fig.3.9. (a) Composite map of the winter (December, January, and February) mean SSTA for the CP (central Pacific) El Niño years in the 1990s (1991/92, 1992/93, and 1993/94), and (b) for the CP El Niño years in the 2000s (2001/02, 2002/03, and 2004/05). Dotted areas reflect a 90% confidence for composite anomalies. 47

Fig.3.10. Nino3 (upper panel) and Nino4 (lower panel) time series (blue bars) decomposed into contributions from the global warming (green bars), low-frequency variability (red curves), and biennial oscillation (blue line) modes. The dashed gray line represents the sum of the three modes. The boxes in the upper panel denote years of strong EP (eastern Pacific) El Niño events and those in the bottom panel denote years of strong CP El Niño events. 49

Fig.4.1. The first CSEOF loading vector of the 31-year (1980-2010) monthly SST anomalies over the tropical Pacific (100°E-80°W, 30°S-20°N). ... 57

- Fig.4.2.** The first CSEOF loading vector of the 31-year (1980-2010) monthly SST anomalies over the North Pacific (100°E-80°W, 20°N-60°N). 58
- Fig.4.3.** The first CSEOF PC time series of the tropical Pacific SST anomaly (solid line, corresponding to the loading vector in Fig. 4.1) and North Pacific SST anomaly (dashed line, corresponding to the loading vector in Fig. 4.2). The vertical dashed line indicates the year 1999. 59
- Fig.4.4.** The first CSEOF loading vector of the tropical Pacific (100°E-80°W, 30°S-20°N) SST anomaly during the period 1980-1998. The North Pacific (100°E-80°W, 20°N-60°N) region depicts the regression of the SST anomaly onto the first CSEOF loading vector in the tropical Pacific. Each panel represents the seasonal mean spatial pattern. 64
- Fig.4.5.** The same map as in Fig. 4.4 but for the period 1999-2010. 65
- Fig.4.6.** Composite map of the reconstructed first CSEOF loading vectors of the tropical Pacific SSTA. Left panel shows composite of El Niño years in the first period (1982/1983, 1986/1987 and 1997/1998) and right panel shows that of the second period (2002/2003, 2004/2005 and 2009/2010). 66
- Fig.4.7.** The first CSEOF loading vector of the tropical Pacific (100°E-80°W, 10°S-20°N) SST anomaly (shaded) for (a) winter (January and February), (b) spring (March to May), and (c) summer (June to August) during the period of 1980 to 1998. The 1000-hPa geopotential height anomaly (100°E-60°W, 10°S-70°N, contour) and the North Pacific SST anomaly (100°E-80°W, 20°N-60°N, shading) are obtained from a regression analysis onto the first CSEOF loading vector of the tropical Pacific SST anomaly. 70
- Fig.4.8.** A regression map of the 1000-hPa wind anomaly (vector) and net surface heat flux anomaly (shaded) for a) winter, b) spring and c) summer corresponding to the first CSEOF loading vector of tropical Pacific SST during the period 1980-1998. Note that the vector scale is different for each panel. 71
- Fig.4.9.** The same map as in Fig. 4.7 but for the period 1999-2010. 77

Fig.4.10. The same map as in Fig. 4.8 but for the period 1999-2010.	78
Fig.4.11. A regression map of the vertical cross-section for the latitude-height geopotential height (shaded) and wind (vector) field averaged over the longitude band from 150° to 170°W for a) winter, b) spring and c) summer corresponding to the first CSEOF loading vector of tropical Pacific SST during the period 1980-1998.	83
Fig.4.12. The same map as in Fig. 4.11 but for the period 1999-2010.	84
Fig.5.1. The first CSEOF loading vectors of the 31-year (1980-2010) monthly SSTA in the Bering and Chukchi Seas (160°E-160°W, 54°-76°N). Each spatial pattern represents the seasonal (3-month) average of the loading vectors.	92
Fig.5.2. The CSEOF PC time series of the Bering and Chukchi SST anomaly (black bar, corresponding to the loading vectors in Fig. 5.1) and North Pacific SST anomaly (blue line, corresponding to the loading vector in Fig. 5.3). The vertical dashed line indicates the year 1999.	93
Fig.5.3. The first CSEOF loading vectors of the 31-year (1980-2010) monthly SSTA in the North Pacific (100°E-80°W, 20°-80°N). Each spatial pattern represents the seasonal (3-month) average of the loading vectors.	94
Fig.5.4. Seasonal (3-month) averages of the first CSEOF loading vector of the SSTA in the Bering and Chukchi Seas (160°E-160°W, 54°-76°N) for 1999-2010.	100
Fig.5.5. The regressed patterns of SIC anomalies (contour) and net surface energy flux anomalies (shading) onto the first CSEOF mode of the Bering and Chukchi Seas SSTA during 1999-2010. The energy flux anomaly is defined as positive in the upward direction.	101
Fig.5.6. The regressed patterns of the 1000-hPa air temperature anomalies onto the first CSEOF mode of the Bering and Chukchi Seas SSTA during 1999-2010.	102

Fig.5.7. The patterns of 1000-hPa geopotential height (contour), wind (vector) and the air temperature (shading) anomalies over the North Pacific (100°E-80°W, 20°-85°N) for (a) December, (b) January, (c) February, and (d) March regressed onto the first CSEOF mode of the Bering Sea SSTA for 1999-2010 (left panel), and the vertical sections of the regressed geopotential height (contour), air temperature (shading) anomalies averaged over the longitude band of 180°-140°W (right panel).
 106

Fig.5.8. The difference (SIC_Run minus Clim_Run) in the SST (shading) and SIC (contour) boundary conditions. Each spatial pattern represents the seasonal (3-month) average of the difference of the boundary conditions.
 110

Fig.5.9. (a) The SIC_Run minus Clim_Run difference of the January and February mean 1000-hPa geopotential height (contour), wind (vector) and air temperature (shading) anomalies over the North Pacific (100°E-80°W, 20°-85°N) and (b) the difference (SIC_Run minus Clim_Run) of the vertical cross-section of the geopotential height (contour), air temperature (shading) averaged over the longitude band 180°-140°W. Plotted here are the differences divided by the standard deviation of the first CSEOF PC time series of the Bering Sea SSTA. (c) The January-February mean regressed patterns of 1000-hPa geopotential height, wind and air temperature anomalies and (d) the vertical sections of the geopotential height and air temperature. 111

Fig.5.10. The regressed patterns of the 1000-hPa geopotential height anomaly (contour) and SST anomaly (shading) corresponding to the first CSEOF loading vector of the Bering and Chukchi SSTA during the period 1999-2010. Seasonal (3-month) average patterns are represented. Note that contour interval is different for each panel. 116

Fig.5.11. The regressed patterns of the 1000-hPa wind anomaly (vector) and net surface energy flux anomaly (shading) corresponding to the first CSEOF loading vector of the Bering and Chukchi SSTA during the period 1999-2010. The seasonal (3-month) average spatial patterns are represented. Note that vector scale is different for each panel. 117

Chapter 1. Introduction

1.1. Background

Interannual to decadal climate variability in the atmosphere and the ocean over and around the Pacific Ocean has attracted considerable attention in the past decade. Since the Pacific Ocean covers approximately one-third of the earth's surface, climate variability in this region has a profound impact on the global weather pattern, marine ecosystem, and the society. Therefore, it is important to understand clearly the mechanism and predictability of the climate variability in the Pacific.

The most prominent climate variability over the Pacific is El Niño-Southern Oscillation (ENSO). The ENSO phenomenon, which features positive sea surface temperature (SST) anomalies in the tropical central and eastern Pacific, is known to exert a profound influence on the entire global climate system. Bjerknes (1969) was the first investigator who recognized that interactions between the ocean and the atmosphere in the tropical Pacific constitute ENSO, and he proposed that ENSO is a strongly coupled ocean-atmosphere phenomenon. Due to the pioneering work of Bjerknes (1969), ENSO research has made remarkable progress in recent years and the scientific community has now reached a general consensus on the fundamental features that contribute to the ENSO phenomenon (see reviews

by Rasmusson and Carpenter 1982; Neelin et al. 1998). For example, ENSO exhibits oscillatory behavior in the tropical Pacific ocean-atmosphere system. It is widely accepted that the occurrence frequency of ENSO peaks in approximately 3- to 5-year periods. In addition, a secondary peak at approximately 2-year periodicity was noted by Rasmusson et al. (1990). The 2-year peak is referred to as the biennial oscillation component. The delayed oscillator hypothesis, which emphasizes the propagation of equatorially trapped waves, is thought to be an important driving mechanism for the oscillatory behavior of ENSO (Suarez and Schopf 1988; Battisti and Hirst 1989). A recharge-discharge oscillator was proposed as a transition mechanism for warm water El Niño events and cold water La Niña events in the eastern Pacific in association with dynamic mass exchange between equatorial and off-equatorial regions (Jin 1997a; Jin 1997b).

Meanwhile, the climate over the North Pacific is largely dominated by decadal or low-frequency variability (Hare and Mantua 2000; Mantua et al. 1997; Trenberth 1990; Trenberth and Hurrell 1994). A widely cited index for low-frequency climate variability over the North Pacific is the Pacific Decadal Oscillation (PDO) (Mantua et al. 1997), which is defined as the leading empirical orthogonal function (EOF) of monthly SST anomalies north of 20°N (available online at <http://jiaso.washington.edu/pdo/PDO.latest>). The

pronounced low-frequency variability is clear in the PDO index, with significant phase transitions from negative to positive values in 1924/25 and in 1976/77, and from positive to negative values in 1947/48 and in 1998/99. The PDO is linked to atmospheric variability in the Aleutian Low and downstream changes in North American winter weather (e.g., Latif and Barnett 1996) and changes in marine ecosystems (e.g., Mantua et al. 1997).

An understanding of the physical mechanisms connecting the tropical Pacific and the North Pacific is essential to address the underlying climate dynamics of atmospheric-oceanic variability in the Pacific basin. Many studies have suggested that ENSO-driven large-scale atmospheric teleconnection alters SST over the North Pacific. In other words, the atmosphere acts as a bridge linking the tropical Pacific and the North Pacific during the ENSO; this process was termed the “atmospheric bridge mechanism” (Alexander 1990, 1992a, 1992b; Alexander et al. 2002; Deser and Blackmon 1995; Lau and Nath 1996, 2001; Zhang et al. 1996). Alexander (1990, 1992a, 1992b) and Alexander et al. (2002) argued that the ENSO-related atmospheric anomalies over the mid-latitudes are characterized by changes in the Aleutian Low in terms of its strength and position. The North Pacific SST anomalies are induced by the alteration of the surface energy fluxes there as a result of strengthened cyclonic surface

winds associated with the stronger Aleutian Low. Lau and Nath (1996, 2001) also demonstrated that the “atmospheric bridge mechanism” is a key process of SST changes in the North Pacific during an El Niño event via simulations using a coupled general circulation model. These authors found that ENSO-related atmospheric circulation anomalies play a significant role in the formation of SST anomalies in the North Pacific through the changes in surface heat fluxes.

In summary, the prevailing paradigm of prominent Pacific climate variability consists of three components: (1) the El Niño/Southern Oscillation (ENSO) in the tropical Pacific; (2) low-frequency or decadal variability in the North Pacific; (3) ENSO-driven atmospheric teleconnections over the North Pacific in regard to the Aleutian Low. These major climate patterns in the Pacific seem to have undergone a significant change recently due possibly to global warming or multi-decadal natural variability. Several studies have suggested that the new features of variability in the North Pacific and in the tropical Pacific were observed in the recent decade, reflecting potentially a new climate regime in the Pacific.

A large portion of the low-frequency fluctuation over the North Pacific has been generally explained by the variation of PDO, which is a dominant SST mode of the North Pacific. Di Lorenzo et al. (2008), however, defined the

new pattern of the North Pacific climate, the North Pacific Gyre Oscillation (NPGO), which is formally defined as the second leading mode of northeast Pacific sea surface height anomalies. This pattern explains a significant fraction of the low-frequency fluctuations not explained by the PDO. Moreover, it was discovered that the NPGO amplitude was larger than the PDO amplitude during the recent decade (Bond et al. 2003; Di Lorenzo et al. 2008, 2010). The ENSO, which is the most prominent mode over the tropical Pacific, also experienced a significant change in its characteristics during the recent decade. The El Niño events occurred in the 2000s were characterized by the SSTA confined to the tropical central Pacific, which is clearly distinguishable from the canonical eastern Pacific El Niño (Kug et al. 2009; Lee and McPhaden 2010; Yeh et al. 2009). This new type of El Niño is termed the central Pacific (CP) El Niño (Kao and Yu 2009), also referred to as the dateline El Niño (Larkin and Harrison 2005), El Niño Modoki (Ashok et al. 2007), or warm-pool El Niño (Kug et al. 2009). Yeh et al. (2009) have predicted that the CP El Niño increase in frequency and magnitude under the future climate change condition. Recent studies have suggested another model for the relationship between the tropical Pacific and the North Pacific. Vimont et al. (2001, 2003a, 2003b) proposed the so-called “seasonal footprinting mechanism” and suggested that mid-latitude atmospheric

variability influences tropical SST variability by producing zonal wind stress anomalies in the subtropical and tropical Pacific. According to Vimont et al. (2003b), winter atmospheric variability in the mid-latitude with a spatial structure resembling the North Pacific oscillation (NPO) (Rogers 1981) imparts an SST “footprint” onto the ocean via changes in the surface heat flux. The subtropical portion of the SST footprint, in turn, forces zonal wind stress anomalies along the equator. Ultimately, the coupled tropical atmosphere-ocean system responds to the zonal wind stress anomalies, producing a central tropical Pacific warming by the end of spring/summer.

In summary, the three prominent components for the Pacific climate variability (i.e., ENSO, low-frequency variability over the North Pacific, and link between the tropical Pacific and the North Pacific) appear to be experienced a significant change in their physics and nature during the recent decade (2000s). That is, 1) the CP El Niño has occurred more frequently and 2) the NPGO amplitude has been generally larger than the PDO amplitude during the 2000s. 3) Also, these changes may be related to the altered physical connection between the tropical Pacific and the North Pacific in recent decade.

1.2. Objectives of the thesis

As mentioned above, the distinct changes in the climate variability over the tropical Pacific and the North Pacific during the recent decades have been well documented in the previous studies. The scientific community, however, has not yet reached a general consensus on the primary physical mechanisms for these climate changes over the Pacific. In particular, there exist widely different views whether these changes are attributed to the anthropogenic global warming signal or these are just one part of the natural low-frequency climate variability.

Based on the research background, this thesis aims to address the outstanding features of the recent climate variability over the Pacific and to identify their physical mechanism. In order to achieve the objectives of the thesis, the decomposition of the data in terms of basis function is very useful in understanding the intrinsic physics of the variability in a dataset. The major statistical tool for decomposing dataset into less complicated categorical modes used in this thesis is the cyclostationary empirical orthogonal function (CSEOF) analysis (Kim et al. 1996; Kim and North 1997).

In the first part of the thesis (chapter 3), intrinsic modes of SST variability are extracted from a 140-year SST reconstruction dataset covering near-global domain via CSEOF analysis for the purpose of

delineating characteristics of the Pacific climate variability and their recent changes. Three modes are identified: a global warming mode, a low-frequency variability mode, and a biennial oscillation mode. It is identified that these three modes constitute the major physical mechanisms for ENSO variability. The primary goals of the first part of the thesis are to substantiate the physical mechanisms driving these three modes of behavior and to demonstrate how these modes jointly contribute to the unique characteristics of recently observed ENSO events. In particular, two key points are addressed in the first part of the thesis; (1) the most extreme El Niño episodes in more than a century occurred during recent decades (e.g., 1982/83 and 1997/98); and (2) the intensity and occurrence frequency of CP El Niño events has increased since the 1990s. Furthermore, the results demonstrate that the CP El Niño events in the 1990s and 2000s have different physical mechanisms. According to the variability of the three modes, the different physical mechanism of the CP El Niño events in the 1990s and 2000s is largely attributed to the different phase of the low-frequency variability mode in 1990s and 2000s (i.e., the phase transitions occurred in 1998/99 from a cold to a warm phase).

In the second part of the thesis (chapter 4), the major focus is on the most recent decadal changes that have occurred in 1998/99. In particular,

analyses of the 31-year atmospheric and oceanic dataset spanning 1980 to 2010 revealed that there are remarkable differences in the relationships between the tropical Pacific and the North Pacific before and after the late 1990s. In the earlier period, the connection between the tropical Pacific and the North Pacific is dominated by the “atmospheric bridge mechanism”, whereas the “seasonal footprinting mechanism” becomes more important in describing the relationship between the tropical Pacific and the North Pacific in the later period. Thus, the primary objective in the second part of the thesis is to demonstrate the distinguishable changes in the ENSO-related SST variability over the North Pacific and the associated atmospheric circulation patterns before and after late 1990s. The physical mechanisms of the changes described above are also to be addressed.

There should be many diverse factors that lead to distinctive climate condition over the Pacific in 2000s, one of which appears to be the global warming signal. In the third part of the thesis (chapter 5), it will be investigated whether the Pacific climate variability in 2000s originated from the global warming or are simply an expression of multi-decadal natural variability. In this context, the relationship between the recent warming in the sub-arctic Pacific and the Pacific climate variability is investigated. In particular, recent warming in the Bering Sea is found to be closely

associated with major atmospheric variability in the North Pacific. Therefore, understanding of the physical connection between the warming in the Bering Sea and the large-scale circulation in the North Pacific is the goal of the third part of the thesis.

In summary, the goals of the present research are as follows:

1. Decompose the Pacific climate variability into physically independent dominant modes (chapter 3).
2. Interpret the physical mechanism of the ENSO events and their recent changes in terms of the interplay originating from the dominant modes of variability (chapter 3).
3. Investigate the decadal changes in the relationship between the tropical Pacific and the North Pacific that occurred in 1998/99 (chapter 4).
4. Identify the relationship between the warming in the Bering Sea and Pacific climate variability during the period of 1999-2010 (chapter 5).

Chapter 2. Data and Methodology

2.1. Data

A monthly mean oceanic and atmospheric dataset were used in the present research. The monthly mean SST data on a 2° longitude \times 2° latitude grid were obtained from the Extended Reconstruction SST version 3 (ERSST.v3) (Smith et al. 2008). In the ERSST.v3, which is the most recent version of the ERSST analysis, optimized reconstruction parameters were applied to improve the low frequency tuning to make the dataset suitable for long-term global-scale studies. The SST anomaly (SSTA) was obtained by subtracting the monthly mean climatology. The monthly mean sea ice concentration (SIC) data were acquired from the Hadley Centre sea ice and SST dataset, version 1 (HadISST1) (Rayner et al. 2003), which is archived at the UK Meteorological Office. The monthly mean atmospheric fields including geopotential heights, zonal and meridional winds, and air temperatures at the standard levels from 1000 to 200 hPa are derived from the National Centers for Environmental Prediction/Department of Energy (NCEP/DOE) reanalysis 2 dataset (Kanamitsu et al. 2002) at a horizontal resolution of 2.5° longitude \times 2.5° latitude. In order to investigate the long-term atmospheric variability, atmospheric data from 1871 to 2010 are analyzed by taking advantage of the 20th Century Reanalysis, version 2

(Compo et al. 2011), which is provided by the NOAA-CIRES (National Oceanographic and Atmospheric Administration-Cooperative Institute for Research in Environmental Sciences) Climate Diagnostics Center.

2.2 Methodology

To extract the principal modes of climate variability, a CSEOF analysis (Kim et al. 1996; Kim and North 1997) is applied to both the oceanic and the atmospheric dataset. In this method, space-time data, $T(r, t)$, are decomposed into cyclostationary loading vectors, $LV_n(r, t)$, and their corresponding principal component time series, $PC_n(t)$, as in (1):

$$T(r, t) = \sum_n LV_n(r, t)PC_n(t). \quad (1)$$

The index n indicates that the data have been decomposed into a number of CSEOF loading vectors and their evolutions. The CSEOF loading vectors are time dependent and periodic, that is,

$$LV_n(r, t) = LV_n(r, t + d), \quad (2)$$

where d , called the nested period. Thus, the CSEOF loading vectors describe temporally evolving physical processes within the nested period, whereas the PC time series represent the temporally varying strengths of the corresponding physical processes. In other words, there are two different types of time dependence in the CSEOF decomposition: one tied with

physics described in $LV_n(r, t)$ and the other tied with the amplitude modulation of physics described in $PC_n(t)$. This method has a considerable advantage of describing the evolution of spatial patterns of physical process throughout the nested period, which is the most distinctive aspect of the CSEOF technique, when compared to other traditional eigenvector analyses.

As hinted above, determining the nested period is an important step for conducting CSEOF analysis. Since there are several physical processes that exist in a dataset, the nested period should be determined such that all of the distinct periods of physical processes are covered. Specifically, this period is the least common multiple of all physical periods (not occurrence periods) in a given dataset. In chapter 3, the nested period is set to 2 years in order to decompose the 140-year SST variability into physically independent modes; this decision is based on the biennial tendency of ENSO (Rasmusson et al. 1990). A detailed interpretation of the nested period is described in Kim (2002), and that study provided a reasonable physical explanation for tropical Pacific SST variability with a 2-year nested period. In chapter 4 and 5, however, the nested period is set to 1 year (12 months) because the analyzed period (1980-2010) is relatively short to apply 2-year nested period. The detailed physical and dynamical interpretations of the

CSEOF method can be found elsewhere (Kim and Roh 2010; Kim et al. 2010; Lim and Kim 2007; Seo and Kim 2003).

To find physically and dynamically consistent modes among different variables, a regression analysis in CSEOF space are conducted. First, CSEOF analysis is performed independently on each variable. Then, the PC time series of the first few significant modes of a predictor variable are regressed onto a PC time series of target variable; that is,

$$PC_n(t) = \sum_{m=1}^M \alpha_m PCP_m(t) + \varepsilon_n(t), \quad (3)$$

where $PCP_m(t)$ are the predictor PC time series, α_m are the regression coefficients, and $\varepsilon_n(t)$ is the regression error time series. The regression coefficients are determined such that the variance of the regression error $\varepsilon_n(t)$ is minimized. The degree of fitting for each mode is measured by the R^2 value, which is given by $1 - \text{var}[\varepsilon_n(t)]/\text{var}[PC_n(t)]$. If the value of R^2 approaches unity, the target and the predictor time series become identical. The regressed spatial patterns of the predictor variable, $LVPR_n(r, t)$, are obtained using the regression coefficients obtained in Eq. (3):

$$LVPR_n(r, t) = \sum_{m=1}^M \alpha_m LVP_m(r, t), \quad (4)$$

where $LVP_m(r, t)$ represents the CSEOF loading vectors of the predictor variable.

As a result of regression analysis in CSEOF space, a predictor variable can be rewritten as:

$$P(r, t) = \sum_n LVPR_n(r, t)PC_n(t). \quad (5)$$

Thus, entire variables can be written as:

$$Data(r, t) = \sum_n \{T_n(r, t), Z_n(r, t), U_n(r, t), V_n(r, t), \dots\} PC_n(t), \quad (6)$$

where the terms enclosed in the brackets denote the evolution of the n th mode as was manifested by the different variables. Evolutions in the different variables are considered to be physically consistent with each other.

Chapter 3. Global warming, low-frequency variability, and biennial oscillation

This chapter presents the primary global modes of SST variability for delineating ENSO characteristics and recent changes in ENSO events. While ocean-atmosphere interactions can explain the principal features of ENSO, observed characteristics of ENSO exhibit considerable irregularities. El Niño or La Niña events are often dissimilar from each other in terms of their amplitude and evolution pattern. Even over the past few decades, each ENSO event has had different characteristics. The uniqueness of each ENSO event makes it difficult to comprehend the intrinsic nature of ENSO. One way to better understand the nature of ENSO is to decompose SSTs into less complicated categorical modes. Barnett (1991), for example, assumed that ENSO events correspond to three time-scale processes, that is, an annual cycle, a quasi-biennial oscillation, and a lower frequency variation pattern. Latif et al. (1997) also identified three modes for tropical Pacific SST variability through the use of a principal oscillation pattern (POP) analysis. These modes included an interannual mode, a decadal mode, and a trend or unresolved ultra-low frequency variability pattern. Kim (2002) decomposed tropical Pacific SST variability into two dominant modes—a biennial mode

and a low-frequency mode—through the use of a cyclostationary empirical orthogonal function (CSEOF) analysis.

In this chapter, intrinsic modes of SST variability are extracted from a 140-year SST dataset covering 70°S–70°N via CSEOF analysis. Three modes are identified: a global warming mode, a low-frequency variability mode, and a biennial oscillation mode.

3.1. Three fundamental modes of SST variability

a. Global warming mode

Dominant modes of SST variability over the near-global domain (0°–360°E, 70°S–70°N) during a 140-year period (1871–2010) are calculated using CSEOF analysis. Figure 3.1 represents the first CSEOF mode of SSTAs, which explains approximately 24% of the total variance in the dataset. Since the nested period is set to 2 years, each CSEOF loading vector depicts SSTA patterns for 24 months. For the sake of brevity, 3-month averaged SSTA patterns are presented in Fig. 3.1a. As shown in Fig. 3.1a, positive SSTAs are found everywhere except for in a relatively small region of the central North Pacific and the North Atlantic where subtle negative SSTAs are observed. Warming is conspicuous in the northern Indian Ocean, the tropical Pacific Ocean, and the southern Atlantic Ocean. These global warming patterns do

not exhibit significant monthly evolution. The corresponding PC time series (Fig. 3.1b) shows a clear increasing trend since 1910, indicating that this mode contains a global SST warming signature.

Strikingly, the warming pattern in the tropical Pacific features an El Niño-like signal with stronger warming in the eastern tropical Pacific than in the western tropical Pacific. Recently, the issue of tropical Pacific SST responses to global warming has received much attention. While it is still controversial whether or not the SST responses are El Niño like (i.e., stronger warming in the tropical eastern Pacific) or La Niña like (i.e., stronger warming in the tropical western Pacific), the majority of the climate models project El Niño-like warming in response to increasing greenhouse gas concentrations in the atmosphere (Meehl and Washington 1996; Timmermann et al. 1999; Cai and Whetton 2000; Boer et al. 2004; Collins 2005). The most plausible and widely accepted mechanism for El Niño-like warming was suggested in Meehl and Washington (1996). This study proposed that negative cloud-albedo feedback in the western Pacific warm pool region could be responsible for stronger warming in the tropical eastern Pacific, which would create an El Niño-like pattern. Both the El Niño-like warming pattern and the increasing PC time series associated with the first CSEOF mode signify a warming signal in the historical dataset.

It should be noted, however, that the PC time series of the first CSEOF mode does not depict a linear trend; there appears to be multi-decadal as well as interannual variability superimposed on the warming trend (Fig. 3.1b). These data imply that the first CSEOF mode does not merely reflect a linear trend in the historical SST dataset. Likewise, Deser et al. (2010) examined linear SST trends in several historical SST datasets over the period of 1900–2008, and the extracted SST trends in the twentieth century did not exhibit robust El Niño-like warming patterns (see Fig. 3.1 in Deser et al. 2010). Even though a large portion of the first CSEOF mode is associated with increasing SSTs, the first CSEOF mode should not be construed as a linear trend for SSTs.

The SST variability associated with the first CSEOF mode can be easily understood by the corresponding reconstruction of SSTAs. The SSTA field is reconstructed by multiplying the loading vector with the corresponding PC time series (note that the loading vector is periodic). Figure 3.1c shows the longitude-time plot of the reconstructed SSTAs averaged over 5°S–5°N. These results show pronounced warming in the tropical Pacific, which reaches the highest level during the 2000s.

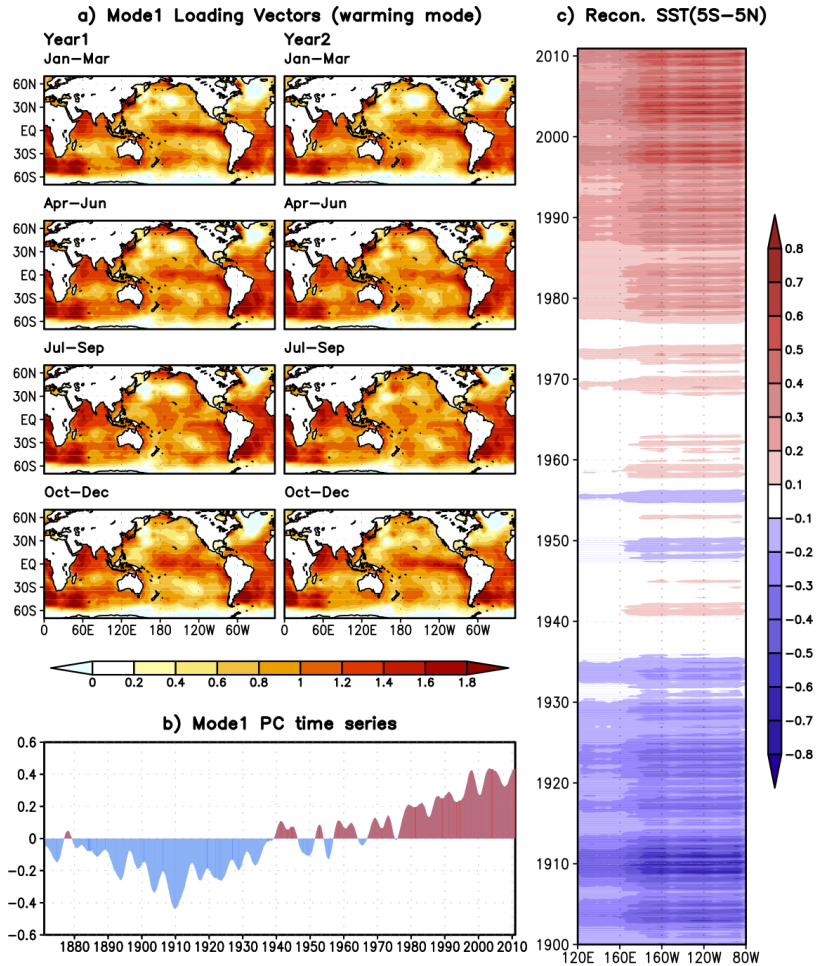


Fig.3.1. (a) The loading vector (0° – 360° E, 70° S– 70° N), (b) the corresponding PC (principal component) time series, and (c) the longitude-time cross section averaged over the equatorial region (5° S– 5° N) for the first CSEOF (cyclostationary empirical orthogonal function) mode of SST (sea surface temperature) anomalies. This mode represents global warming/cooling.

b. Low-frequency variability mode

Figure 3.2 shows the second CSEOF mode, which explains approximately 13% of the total variance in the SST dataset. The spatial pattern of the second CSEOF mode shown in Fig. 3.2a does not change significantly within the nested period. Thus, this mode may be considered to be approximately stationary. The SSTA pattern is quite similar to well-known ENSO features that show strong positive SSTAs over the tropical eastern and central Pacific. There are, however, some notable differences between the second CSEOF mode and conventional ENSO features. The SSTA pattern in the tropical region is broader in the meridional direction than in the conventional ENSO signal, and the positive anomalies extend from the northeastern to the southeastern mid-latitude Pacific. Also, Fig. 3.2a depicts stronger SSTAs in the tropical central Pacific (see also Fig. 3.2c), which correspond to typical features observed during CP El Niño events.

Significant SSTAs appear not only in the tropical Pacific, but also in the North Pacific and South Pacific. Note that the second mode does not account for much of the variance in the Indian and Atlantic Oceans. The SSTA in the south Pacific shows a dipole-like structure in the meridional direction with positive SSTA to the south of 45°S and negative SSTA to the north of 45°S. The SSTA pattern in the North Pacific has a negative anomaly with an

elliptical shape over the western to central North Pacific and a positive anomaly along the eastern North Pacific. This pattern is similar to the structure of the PDO (Mantua et al. 1997), which represents the primary decadal mode of the North Pacific. This similarity can be confirmed through comparisons of the PDO index with the PC time series of the second CSEOF mode (shading in Fig. 3.2b). The PC series is strongly correlated at a 0.64 level with the 2-year moving average data from the monthly PDO index (data not shown). To further investigate characteristics of the second CSEOF mode, correlations between the PC time series and the monthly Nino3 index (SSTA averaged over 90°–150°W, 5°S–5°N) are calculated. Correlation of the two time series is 0.45 (data not shown), and it increases markedly to 0.84 when a 5-year low-pass filter is applied to the Nino3 index after the linear trend is removed (dashed line in Fig. 3.2b).

High correlations of the PC time series with the PDO index and the low-pass filtered Nino3 index suggest that the second CSEOF mode represents a connection between low-frequency variability of the tropical and the North Pacific. There is a growing body of evidence that suggests that the low-frequency variability of ENSO is largely modulated by decadal variability in the North Pacific (Gu and Philander 1997; Latif et al. 1997; Barnett et al. 1999; Kleeman et al. 1999; Pierce et al. 2000; Vimont et al.

2003). In this respect, the second CSEOF mode may signify a link between the tropical Pacific and the North Pacific on interannual and decadal time scales.

Figure 3.2c displays the longitude-time cross section of tropical Pacific (5°S–5°N) SSTAs reconstructed from the second CSEOF mode. The data in this figure show primarily interdecadal fluctuations of tropical Pacific SSTAs, although weak intradecadal variability is also observed. In recent decades, transitions occurred in 1976/77 from a cold to a warm phase, and from a warm to a cold phase in 1998/99. These phase transitions are also evident in the PDO variability. The 1976/77 transition is particularly noteworthy in the PDO index, which has been termed a climatic ‘regime shift’ (Miller et al. 1994). Also, substantial evidence supports the idea that physical conditions in the North Pacific changed around 1998/99 (Minobe 2000; Schwing and Moore 2000; Bond et al. 2003; Peterson and Schwing 2003). The evidence from these studies further confirms that the second CSEOF mode constitutes a connection between the tropical Pacific and the North Pacific on interannual and decadal time scales.

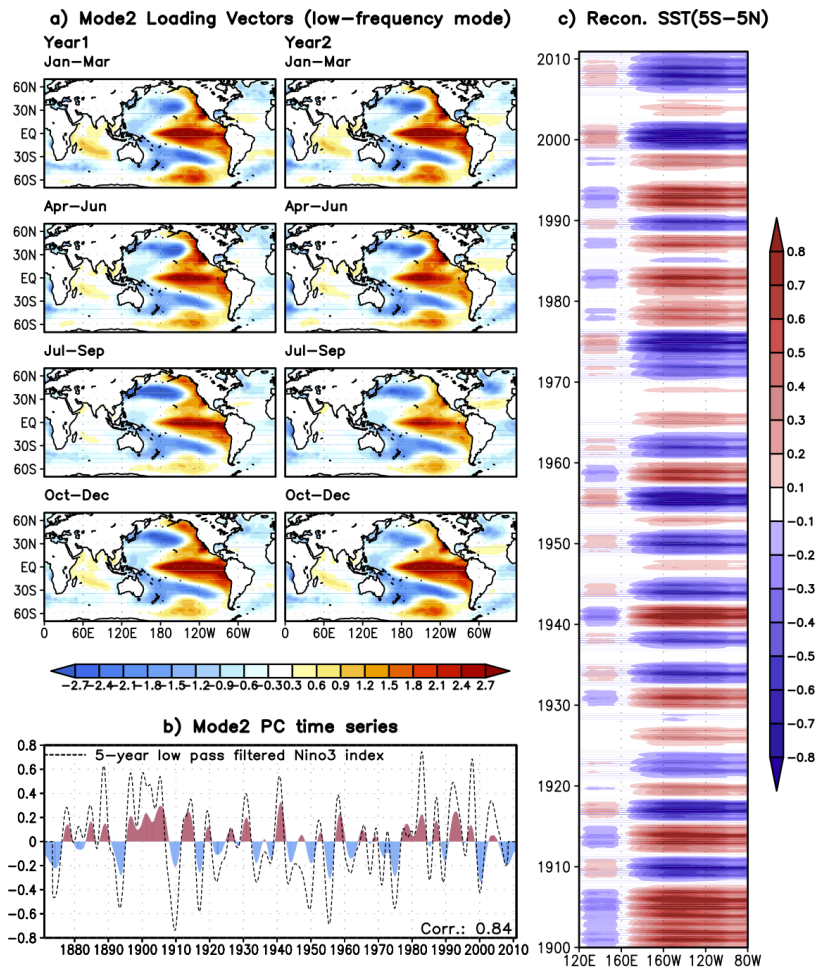


Fig.3.2. The data presented are similar to the data in Fig. 3.1 but are for the second CSEOF mode. The dashed line in (b) represents the 5-year low-pass filtered Nino3 index after removing a linear trend. This mode represents low-frequency SST variability in the Pacific.

c. Biennial oscillation mode

Figure 3.3 shows the third CSEOF mode, which explains approximately 8% of the total variance in the SST dataset. In contrast to the first and the second CSEOF modes, the spatial patterns of the third mode exhibit a clear oscillation within the nested period (Fig. 3.3a). The SSTA evolution patterns portray the development of El Niño and La Niña events and show details of the phase transitions between the two. During the spring (April–June) of year 1, a warm SSTA develops in the eastern tropical Pacific off the coast of Peru. This warm anomaly grows towards the central tropical Pacific during successive months (July–September), and reaches its maximum amplitude by the end of the calendar year (October–December). After El Niño reaches a mature stage, negative feedback mechanisms work to reset the thermocline depth in the tropical Pacific and terminate the El Niño phase. The negative feedback mechanisms are described in the context of a delayed oscillator (Suarez and Schopf 1988; Battisti and Hirst 1989) and a recharge-discharge oscillator (Jin 1997a; Jin 1997b). Subsequently, negative feedback results in cold SST anomalies in the eastern tropical Pacific as is observed during the spring (April–June) of year 2. This negative SSTA develops toward the central tropical Pacific until it matures in the winter (October–December) of year 2.

In addition to the oscillatory nature of the third CSEOF mode, several aspects of the third mode demonstrate that this mode fits the description of a canonical ENSO. First, the intensity of the SST change is confined to a narrow equatorial zone, while the SSTA in the northern North Pacific is relatively weak (Fig. 3.3a). Second, the SSTA over the Indian Ocean lags behind the ENSO signal by about one season. The warm SSTA in the Indian Ocean first appears during the mature stage of El Niño development (October–December in year 1) and peaks during the decaying phase (January–March in year 2). The warm SSTA in the Indian Ocean persists during the transition stage from El Niño to La Niña (April–June in year 2). Previous studies suggested a feedback process between the Indian Ocean SSTA and ENSO that a warming in the Indian Ocean, which is a part of an El Niño signal, plays a role in the transition of an El Niño into a La Niña via easterly wind stress over the western Pacific (Kug and Kang 2006; Yoo et al. 2010; Kim et al. 2011).

The characteristics of the third CSEOF mode described above are classical features associated with conventional ENSO events (e.g., Rasmusson and Carpenter 1982). In fact, this mode is nearly identical to the one identified in Kim (2002). The Kim (2002) study focused on the similarity of the CSEOF mode and the biennial component of the tropical

Pacific variability addressed by Rasmusson et al. (1990). The third CSEOF mode identified in this study, therefore, is termed the biennial oscillation mode following the nomenclature used by Rasmusson et al. (1990).

Figure 3.3c shows the reconstructed SSTAs averaged over the tropical Pacific region. These data confirm that the third CSEOF mode constitutes biennial oscillations of SSTAs in the tropical Pacific, although not all biennial oscillations are necessarily in phase. The PC time series of the third CSEOF mode is presented in Fig. 3.3b, which shows that the amplitude of the biennial oscillation underwent long-term variations.

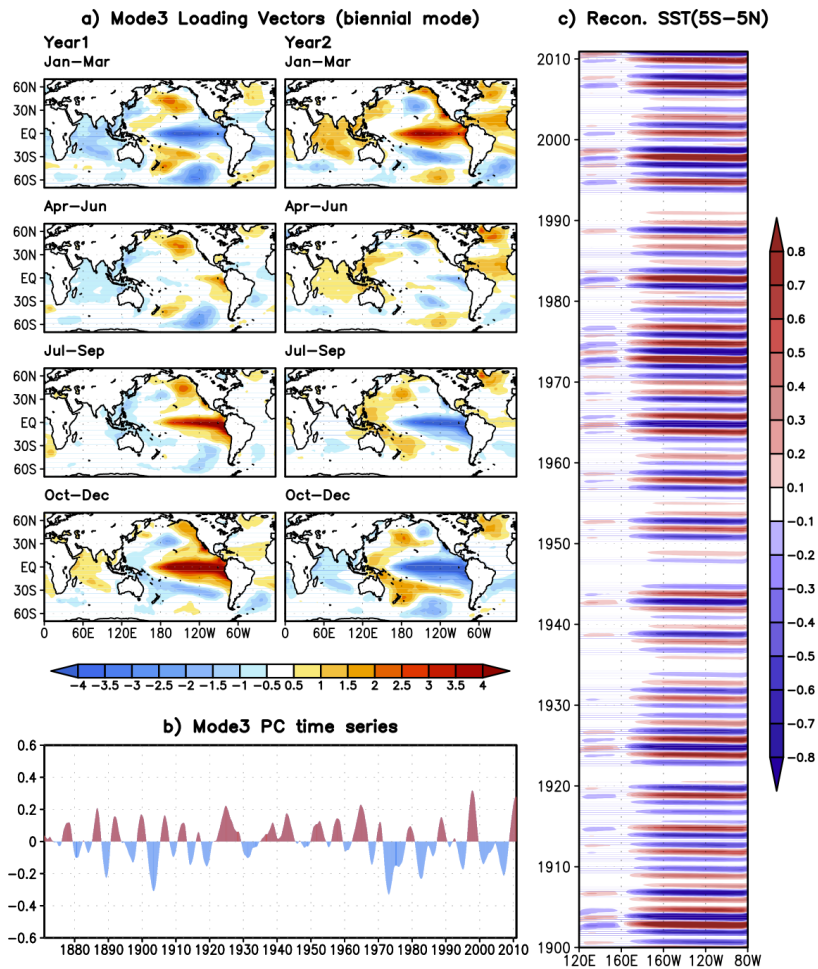


Fig.3.3. The data presented are similar to the data in Fig. 3.1 but are for the third CSEOF mode. This mode represents primarily the biennial oscillations (tendency) of SST in the tropical Pacific.

d. Independence of the three modes and their relevance to tropical Pacific SSTA

The three dominant modes of the near-global SST variability identified via CSEOF analysis are the global warming mode, the low-frequency variability mode, and the biennial oscillation mode. The SSTA evolution patterns in the loading vectors of the three modes are different from each other as was discussed above. In particular, a biennial SSTA phase transition is characteristic of the third CSEOF mode and warm water anomalies are frequent almost every other year. In contrast, the SSTAs associated with the second CSEOF mode exhibit the same sign over two-year periods. Interestingly, the spatial patterns of these two modes are strongly correlated with each other. The differences between the modes could not be realized when the nested period was set to one year. Hence, the nested period is set to 2 years in the present study.

Although the three modes are temporally uncorrelated with each other, they do not necessarily represent independent modes of SST variability. Their independence can be tested by calculating the lead-lag correlation among the PC time series as is plotted in Fig. 3.4. The correlation coefficients between the PC time series of the first and third modes (blue dotted line) and the second and third modes (red dashed line) are

insignificant at a 99% confidence level ($r \approx 0.11$) for almost all lags. Although correlations of the first and second PC time series are not entirely negligible for all lags (black solid line), the correlations are generally insignificant. These results confirm that the three modes are nearly independent of each other. Therefore, the three principal modes of SSTAs extracted via CSEOF analysis seem to have originated from independent sources or were driven by different physical mechanisms of variability.

To examine how much of the total variability of tropical Pacific SSTAs can be explained by the three CSEOF modes, SSTAs are reconstructed by summing the data from three modes and comparing the results to the raw data. Figures 3.5a and 3.5b display the longitude-time cross sections of the SSTAs that are averaged over the equatorial region (5°S – 5°N) for the raw data and the reconstructed data, respectively. The three modes together reasonably reproduce the observed SSTAs, which primarily are associated with ENSO variability. To further confirm this similarity, the Nino3 and Nino4 (160°E – 150°W , 5°S – 5°N) indices from the reconstructed SSTA data (orange curves in Figs. 3.5c and 3.5d) are compared with the original indices from the raw SST anomaly data (black curves in Figs. 3.5c and 3.5d). The correlations between the reconstructed and the raw data are 0.86 and 0.83 for the Nino3 and Nino4 indices, respectively. These results indicate that the

three-mode reconstruction captures a significant portion of the observed ENSO variability. As can be seen in Fig. 3.5, the majority of SST variability over the tropical Pacific can be decomposed into three modes (i.e., the global warming mode, the low-frequency variability mode, and the biennial oscillation mode) that likely originated from statistically independent physical mechanisms.

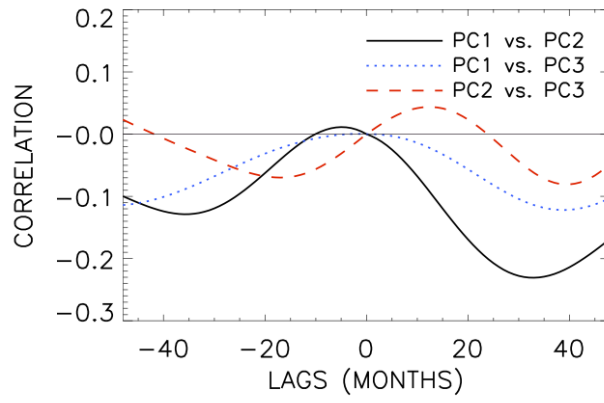


Fig.3.4. Lead-lag correlation among the first three CSEOF PC time series.

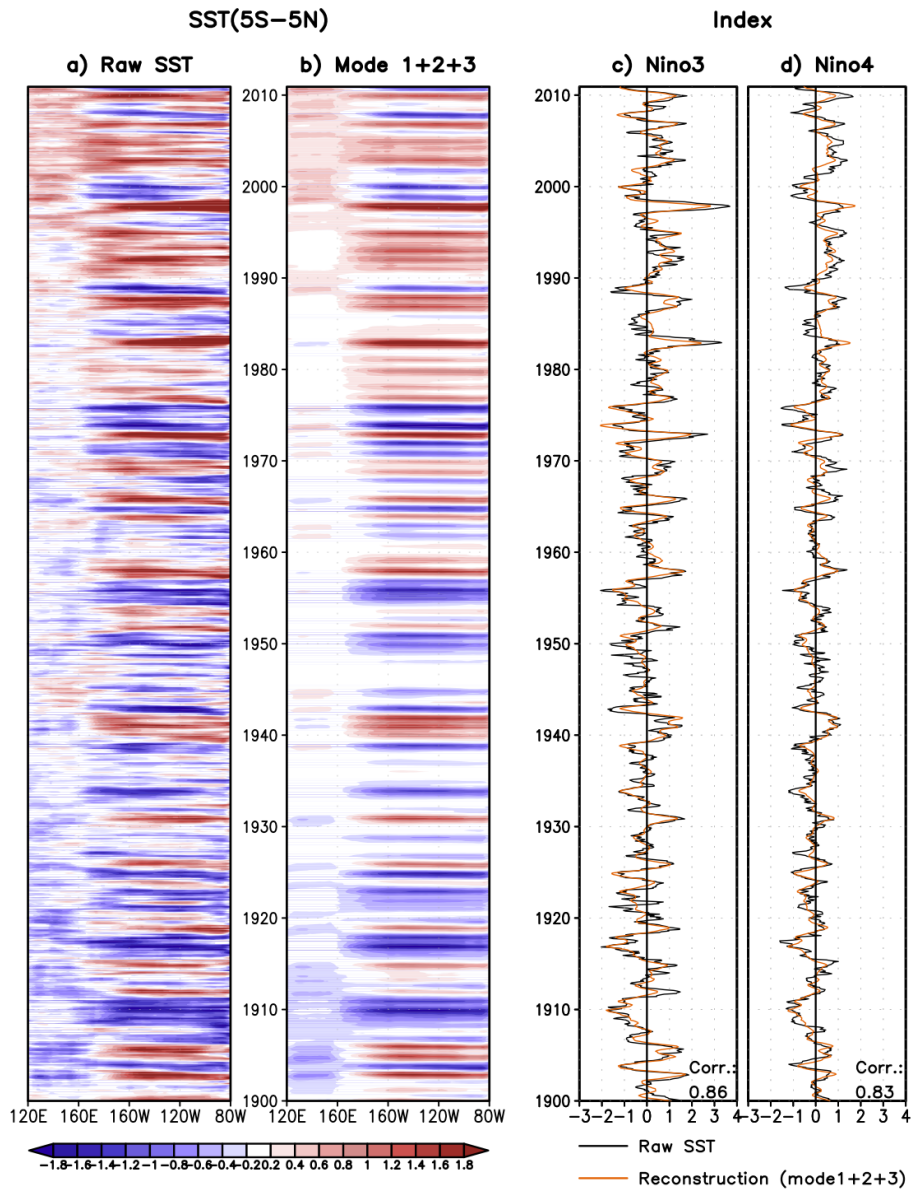


Fig.3.5. Longitude-time cross section of SSTA (SST anomalies) averaged over the equatorial region (5°S-5°N) of (a) the raw data, and (b) the reconstructed data based on the first three modes. (c) Nino3 and (d) Nino4 indices obtained from the raw SSTA data (black line) and the 3-mode SSTA reconstruction (orange line).

e. Distinct physical responses to the three SSTA modes

To examine the atmospheric variability associated with the SSTA for the three CSEOF modes, regression analysis in CSEOF space was conducted. Due to the distinct physical natures of the three modes, atmospheric variability differs significantly in magnitude and pattern among the three modes. Figure 3.6 displays the winter (December, January, and February) patterns of SSTAs for the three modes and the corresponding regression patterns of precipitation anomalies. The spatial patterns are scaled such that the variance of the corresponding PC time series is unity. Thus, the patterns reflect the relative magnitude of anomalies associated with the three modes. While all three modes depict central and eastern tropical Pacific warming (Figs. 3.6a, 3.6b, and 3.6c), the associated precipitation anomaly patterns differ appreciably. For example, the precipitation anomalies associated with the global warming mode differ significantly in pattern and magnitude from those of the other two modes. As shown in Fig.3.6e, the positive anomaly over the equator is quite weak, and is confined to the tropical central Pacific, while the stronger positive precipitation anomaly is elongated to the eastern Pacific in the second and third modes (Figs. 3.6f and 3.6g). The precipitation anomalies corresponding to the low-frequency variability mode and the biennial oscillation mode exhibit similar features—positive anomalies over

the central and eastern Pacific and negative anomalies over the western Pacific (Figs. 3.6f and 3.6g). However, the difference of the precipitation anomalies (Fig. 3.6h) shows that the detailed feature and magnitude of precipitation differs from each other despite the similarity of the SSTA pattern (Fig. 3.6d).

The regression patterns of air temperature, geopotential height, and wind also differ substantially among the three modes (Fig. 3.7). A similarity in SSTA patterns over the tropical Pacific is obvious between the low-frequency variability and the biennial oscillation modes (Figs. 3.6b and 3.6c). Nonetheless, the atmospheric circulation and air temperature patterns associated with these two modes differ appreciably from each other. Previous studies on ENSO-related atmospheric teleconnection revealed that the Aleutian Low becomes stronger during an El Niño event (Lau and Nath 1996; Alexander et al. 2002). As shown in Figs. 3.7b and 3.7c, the Aleutian Low observed at the 1000-hPa level is intensified as expected, but the position and magnitude of the intensification differ between the two modes. The anomalous Aleutian Low in the biennial oscillation mode is centered further northward and covers a smaller area of the North Pacific compared to that in the low-frequency variability mode. Due to different atmospheric circulation patterns, the regressed air temperature anomalies for modes

two and three also differ in pattern and magnitude (shadings in Figs. 3.7b and 3.7c). In the low-frequency variability mode, a positive temperature anomaly prevails over the western United States while a negative temperature anomaly is seen over the southeastern United States. In the biennial oscillation mode, on the other hand, an intense positive temperature anomaly is present over Canada. Significant differences are also observed over the Asian continent. Differences in the atmospheric variability associated with the two modes are shown in Figs. 3.7d and 3.7h. The atmospheric teleconnection patterns for the low-frequency and biennial modes differ critically despite the similarity of the SSTA patterns over the tropical Pacific. Therefore, the distinction of these three modes will be crucial not only for ENSO forecasting, but also for understanding teleconnection patterns and terrestrial responses to ENSO.

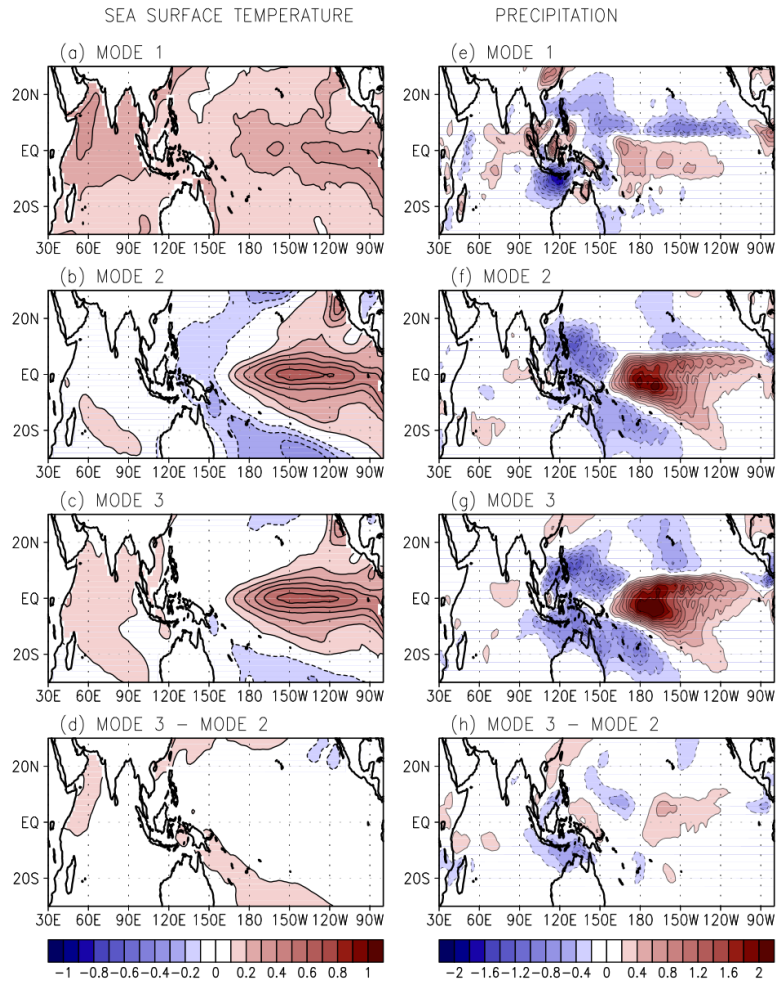


Fig.3.6. The (a) first, (b) second, and (c) third CSEOF loading vectors of SSTA and the map of regressed precipitation anomalies corresponding to the (e) first, (f) second, and (g) third CSEOF modes of the SSTA. The SSTA and precipitation differences between the third and second CSEOF modes (mode 3 - mode 2) are presented in (d) and (h), respectively. The presented patterns represent averages from December to February. The CSEOF and regression patterns are scaled by the standard deviation of the respective PC time series (eigenvalues) so that the PC time series have a unit variance.

3.2. Characterization of recent ENSO events identified by three CSEOF modes

A primary objective in the present chapter is to understand how the three principal modes of SSTAs contribute to the major ENSO events that have occurred in recent years. The contribution of each of the three modes to the observed ENSO variability is presented in Fig. 3.8. Figures 3.8a, 3.8b, and 3.8c display longitude-time cross sections of the three modes of tropical Pacific (5°S – 5°N) SSTAs, respectively, and Fig. 3.8d shows the winter-mean (averages from December to February) Nino3 and Nino4 indices calculated from the raw SSTA data. The data presented in Fig. 3.8 is for the period of 1955–2010, since the main focus of this analysis is on the major ENSO events during the most recent decades. Figure 3.8 provides insight into how the interplay of the three principal modes (i.e., the global warming mode, the low-frequency variability mode, and the biennial oscillation mode) determines the observed characteristics of ENSO events.

The low-frequency variability mode shows multiple phase transitions during the data period analyzed (Fig. 3.8b). Since 1977, a warming trend is clear and it is associated with the global warming mode (Fig. 3.8a). Meanwhile, the magnitude of the biennial oscillation mode varies in time without any obvious trends or phase transitions (Fig. 3.8c). The biennial

oscillation mode exhibits marked warming during strong El Niño years (1982/83 and 1997/98). Note that there is also remarkable warming in the biennial oscillation mode during 1972/73, and that this warm anomaly is larger than those observed in 1982/83 and 1997/98. Nonetheless, the 1972/73 El Niño was not as strong as the 1982/83 or 1997/98 events according to the Niño3 index (Fig. 3.8d). One major difference among the 1972/73, the 1982/83, and the 1997/98 events is found in the low-frequency variability mode. For the 1972/73 El Niño, a strong negative SST anomaly from the low-frequency variability mode offsets a strong positive anomaly from the biennial oscillation mode. As a result, warming during the 1972/73 event turned out to be smaller than the warming during the 1997/98 and 1982/83 events. In contrast, during the 1997/98 El Niño, a positive anomaly from the low-frequency variability mode amplifies the tropical eastern Pacific El Niño signal. A similar pattern also emerges during the 1982/83 El Niño. In addition, the global warming mode contributes positively to these record-breaking El Niño events.

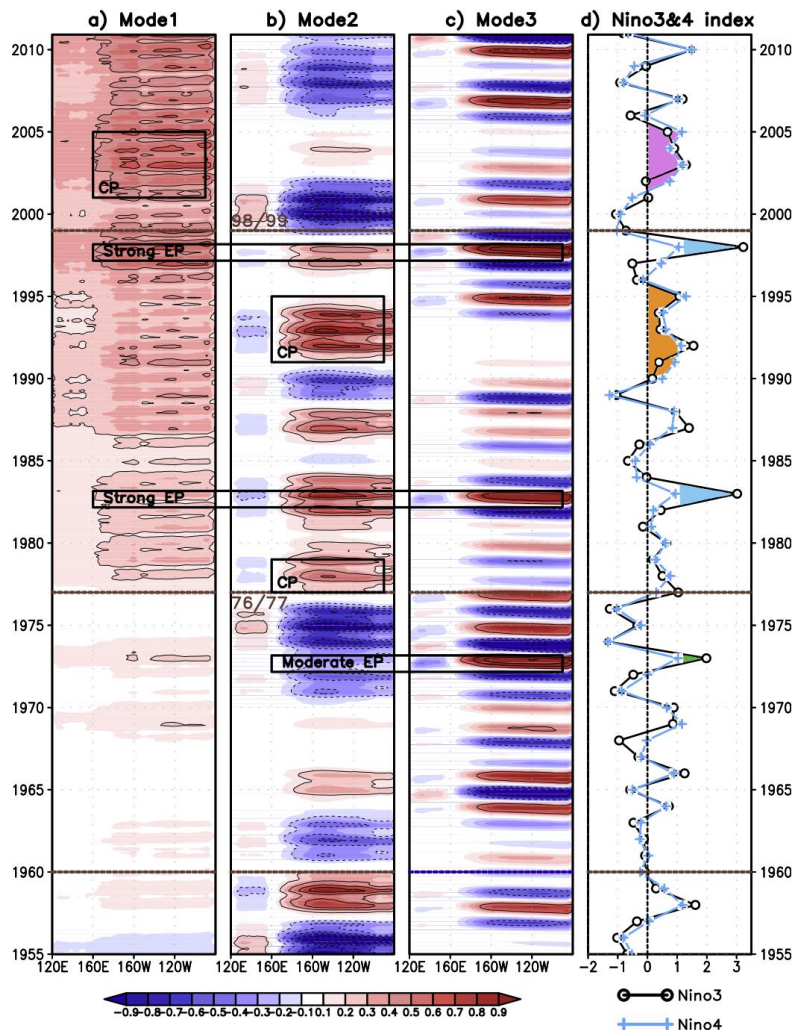


Fig.3.8. Longitude-time cross section of the reconstructed SSTA based on the (a) first, (b) second, and (c) third CSEOF modes. (d) The Nino3 (black line) and Nino4 (blue line) indices of the raw SSTA data. The horizontal lines from top to bottom denote 1998/99, 1976/77, and 1959/60 boundaries, respectively.

The asymmetry observed between El Niño and La Niña, with El Niño warming larger than La Niña cooling, can be understood via the same types of mechanisms that were described above. Negative and positive SST anomalies associated with the biennial oscillation mode are generally comparable in magnitude. Nonetheless, no strong La Niña events were observed during recent decades, since the negative anomalies from the biennial oscillation mode tend to be offset by positive anomalies from the low-frequency variability mode and the global warming mode. Since 1960, there was no instance where all three modes had negative anomalies.

A prolonged warming condition was observed over the tropical Pacific during the first half of the 1990s (orange shading in Fig. 3.8d). Many authors have described this unusual physical condition in detail (Ji et al. 1996; Kleeman et al. 1996; Goddard and Graham 1997; Gu and Philander 1997; Latif et al. 1997; Zhang et al. 1997). Recent studies have focused their attention on the warming that occurred in the CP region during the early 1990s El Niño (e.g., Kug et al. 2009; Yeh et al. 2009). During this period, the low-frequency variability mode shows striking positive anomalies (boxed area in Fig. 3.8b), while the amplitude of the biennial oscillation mode is negligible. Thus, it can be inferred that the warm anomaly in the tropical Pacific during the early 1990s is not associated with equatorial wave

dynamics (Kim and Kim 2002). That is, the tropical warming during this period was not like a conventional ENSO. Rather, the anomalous warming condition originated mainly from the low-frequency variability mode. This interpretation is consistent with Latif et al. (1997), who concluded that the anomalous 1990s were dominated by the decadal mode, which was extracted via POP analysis. In addition, our study suggests that the global warming signal contributed to the anomalous 1990s, although the contribution from the global warming mode was smaller than that from the low-frequency variability mode. This conclusion is different from that of Latif et al. (1997), who concluded that global warming was not responsible for the anomalous 1990s.

As noted above, the sequence of El Niño events during the early 1990s were classified as CP El Niño events in previous studies (Kug et al. 2009; Yeh et al. 2009). These studies defined an event as a CP El Niño if the Nino4 index exceeded the Nino3 index. Note that the Nino4 index is mostly larger than the Nino3 index during the time period ranging from 1990/91 to 1994/95, except for in 1991/92 (Fig. 3.6d). However, even the 1991/92 event has been classified as a CP El Niño according to several studies that used different CP El Niño definitions (Ashok et al. 2007; Kim et al. 2009; Yu and Kim 2010). The CP El Niño signature can be found in the low-frequency

variability mode, with a maximum warming in the tropical central Pacific rather than the tropical eastern Pacific (see the boxed area in Fig. 3.8b and Fig. 3.2a). In particular, the CP El Niño of 1991/92, 1992/93, and 1993/94 conforms to the years of strong low-frequency variability. Similarly, the CP El Niño event during 1977/78 originated from the low-frequency variability mode (see the boxed area in Fig. 3.8b).

The CP El Niño is regarded to have occurred more frequently than the eastern Pacific (EP) El Niño during the 2000s (Yeh et al. 2009; Lee and McPhaden 2010; Yeo et al. 2012). The events in 2001/02, 2002/03, 2004/05, and 2009/10 were classified as CP El Niño events in previous studies (Kug et al. 2009; Yeh et al. 2009; Kim et al. 2009; Yu and Kim 2010). As shown by the Nino3 and Nino4 indices, there was a persistent warming in the tropical Pacific during the earlier 2000s (pink shading in Fig. 3.8d), which looked similar to the warming observed during the earlier 1990s (orange shading in Fig. 3.8d). Even after the linear trend is removed from the Nino3 and Nino4 indices, the prolonged warming during the earlier 2000s is still apparent (data not shown). To clarify the primary cause of tropical Pacific warming during the earlier 2000s, it is examined how the three modes affect the tropical Pacific SSTAs during this time frame. In 1998/99, the low-frequency variability mode transitioned to a cold phase,

but the negative SSTA associated with this mode was insignificant during 2002–2006 (Fig. 3.8b). The amplitude of the biennial oscillation mode was also relatively small during this period. While the biennial oscillation and the low-frequency variability modes were relatively weak, CP El Niño events were observed during this period (pink shading in Fig. 3.8d). Significant warming was seen only in the global warming mode during this period. Hence, the CP El Niño events that occurred during the early 2000s (i.e., 2001/02, 2002/03, and 2004/05) were primarily driven by the global warming mode, and there were little contributions made by the low-frequency variability and biennial oscillation modes.

The latest CP El Niño event occurred in 2009/10. As shown in Fig. 3.8, the 2009/10 CP El Niño was primarily associated with positive anomalies in the global warming and biennial oscillation modes, and there was a relatively weak negative anomaly in the low-frequency variability mode. The sizable contribution from the biennial oscillation mode made the 2009/10 CP El Niño event unique when compared to earlier CP El Niño events. Indeed, Kim et al. (2011) pointed out the unique structure of the 2009/10 CP El Niño. For example, the 2009/10 CP El Niño showed a record-breaking warm SSTA in the central Pacific (see Nino4 index in Fig. 3.8d), which then rapidly decayed to a La Niña state. These characteristics of the

2009/10 CP El Niño appear to be associated with the biennial oscillation mode.

One major point emerges in this section and that is that the CP El Niño events in the early 1990s and the early 2000s appear to be driven by different physical mechanisms. That is, the CP El Niño events in the early 1990s originated mainly from the low-frequency variability mode, while those in the early 2000s were derived mainly from the global warming mode. In order to confirm this difference, composite maps of SSTAs are constructed based on the selected CP El Niño years of the 1990s and those of the 2000s (Fig. 3.9). The years 1991/92, 1992/93, and 1993/94 are selected as CP El Niño years for the 1990s. Similarly, the years 2001/02, 2002/03, and 2004/05 are selected as CP El Niño years for the 2000s. For the composite analysis, SSTAs are calculated based on 1955–2010 climatology and the winter-mean (averages from December to February) anomalies are used. As expected, the CP El Niño composite in the 1990s (Fig. 3.9a) reflects well with the characteristic features of the low-frequency variability mode, with the tropical central Pacific warming extending to the northeastern Pacific and the cold SSTAs in the central North Pacific. Meanwhile, the CP El Niño composite in the 2000s (Fig. 3.9b) clearly depicts a warming pattern consistent with the global warming mode.

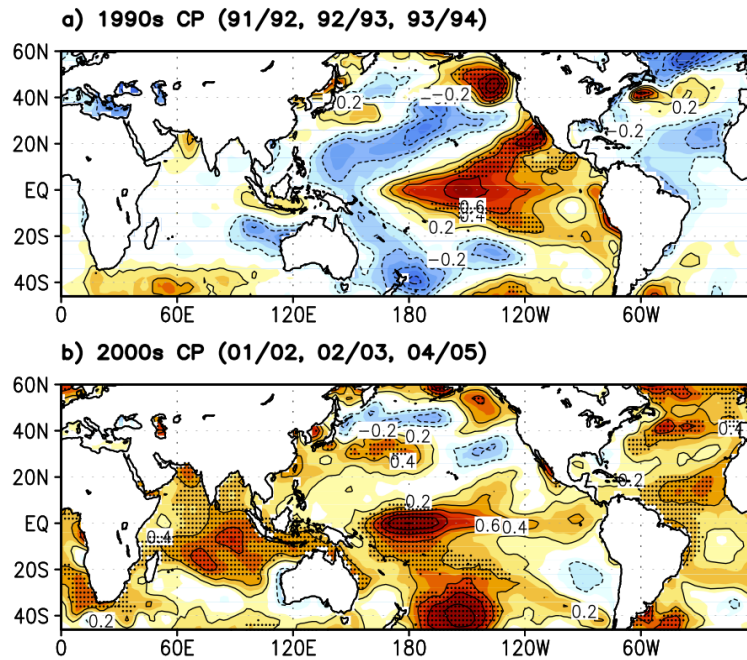


Fig.3.9. (a) Composite map of the winter (December, January, and February) mean SSTA for the CP (central Pacific) El Niño years in the 1990s (1991/92, 1992/93, and 1993/94), and (b) for the CP El Niño years in the 2000s (2001/02, 2002/03, and 2004/05). Dotted areas reflect a 90% confidence for composite anomalies.

A similar statement can be made when SST anomaly is defined with respect to the 1871-2010 climatology (figure not shown).

The Nino3 and Nino4 indices are not found to represent an accurate depiction of physical and dynamical conditions in the tropical Pacific. Hence, the Nino3 and Nino4 indices are likely not appropriate criteria to use for describing physical and dynamical differences between EP El Niño and CP El Niño events. Figure 3.10 shows how the Nino3 and Nino4 indices (blue bars), which merely reflect total SSTA variability over the tropical Pacific, are comprised of distinct contributions from the global warming mode (green bars), the low-frequency variability mode (red curve), and the biennial oscillation mode (blue line). The sum of the three modes (gray dashed line) fit the Nino3 and Nino4 indices well. Each tropical Pacific warming/cooling event consists of a different combination of the three modes. Due to the distinct physical nature of the three modes, it should be imperative to distinguish the disparate sources of warming in the tropical Pacific.

It is identified that the low-frequency and biennial components of the tropical Pacific SST variability constitute the intrinsic feature of ENSO. Recently, however, ENSO characteristics are significantly affected by global warming. How global warming affects ENSO variability can be understood

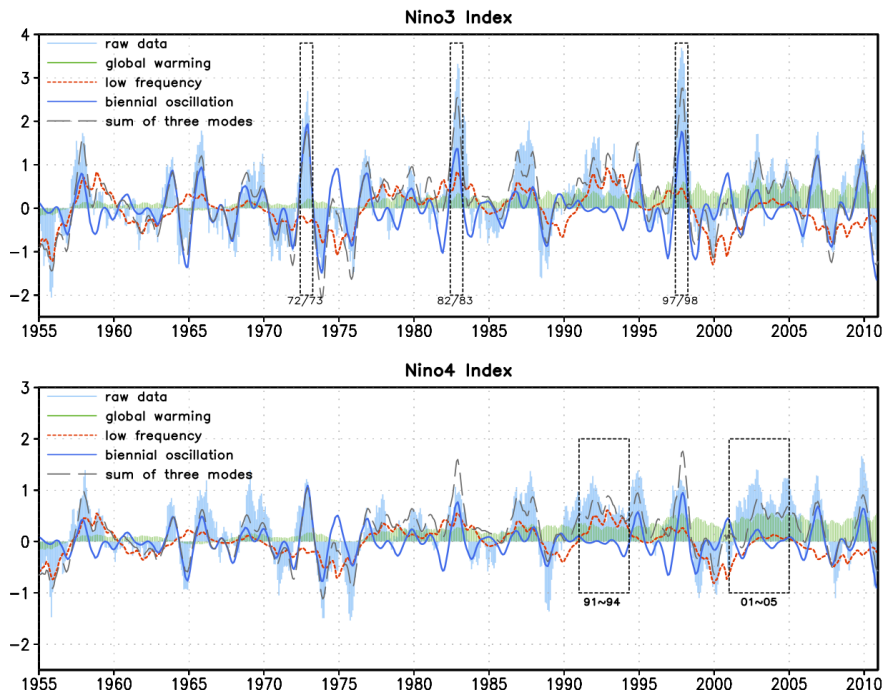


Fig.3.10. Nino3 (upper panel) and Nino4 (lower panel) time series (blue bars) decomposed into contributions from the global warming (green bars), low-frequency variability (red curves), and biennial oscillation (blue line) modes. The dashed gray line represents the sum of the three modes. The boxes in the upper panel denote years of strong EP (eastern Pacific) El Niño events and those in the bottom panel denote years of strong CP El Niño events.

by comparing the ENSO characteristics before 1960 with those in the recent decade. In 1914/15, both the low-frequency variability and the biennial oscillation modes exhibit positive SSTA (see Figs. 3.2c and 3.3c), which is similar to the strong El Niño events in 1982/83 and 1997/98 (see Fig. 3.8). The intensity of the 1914/15 El Niño as measured by the Nino3 index, however, is approximately one-third of that of the 1982/83 El Niño, which is mainly due to the negative sign of the global warming mode.

Several years of negative SSTA in the low-frequency variability mode and positive SSTA in the biennial oscillation mode are identified in the dataset (e.g., 1937/38, 1943/44, 1972/73, 1974/75, 2006/07, and 2009/10). As shown in Fig. 3.1c, the global warming signal is obscure in 1937/38, 1943/44, 1972/73 and 1974/75 events. Thus, these years are classified as non-ENSO years, since the low-frequency and the biennial oscillation modes tend offset each other (see Nino3 or Nino4 indices in Fig. 3.5); an exception is the 1972/73 El Niño when the positive SSTA in the biennial oscillation mode was extremely strong. On the other hand, warming in the tropical Pacific is significant during the years of 2006/07 and 2009/10, despite the opposite sign of SSTAs in the low-frequency variability and biennial oscillation modes (Fig. 3.8). It appears that El Niño events in

these years were strongly affected by the conspicuous global warming signal.

There has been no significant change in the strength of the low-frequency variability and the biennial oscillation modes (red curve and blue line in Fig. 3.10) with the advancement of global warming. As can be seen in the PC time series of the two modes (Figs. 3.2b and 3.3b), there was no indication that these intrinsic features of ENSO have varied in any substantial way over the last 100 years (1910–2010), during which sea surface temperatures in the equatorial Pacific (120°E–80°W, 20°S–20°N) rose by about 0.65°C. There was also no sign of more frequent CP El Niño events or less frequent La Niña events during the last century in the low-frequency variability and the biennial oscillation modes. Hence, it is likely that continued warming in the tropical Pacific was responsible for the apparent increase in the occurrence frequency of CP El Niño events and the decrease in the frequency of La Niña events during recent decades.

An important question to consider is whether or not the results presented here are dependent on the dataset or the analysis period. The results presented in this study are not overly sensitive to the employed dataset. Analyses based on Hadley Centre Sea Ice and Sea Surface Temperature (HadISST) (Rayner et al. 2003) and Kaplan SST (Kaplan et al.

1998) datasets yield virtually identical results to those presented in chapter 3. Even though the three SST datasets (i.e., ERSST.v3, HadISST, and Kaplan SST) have different spatial resolutions, the first three CSEOF modes are quite similar among the three datasets. This level of consistency adds robustness to the results obtained in the present study. Numerous data spanning the twentieth century are typically required to discriminate the global warming signal from decadal fluctuations. Although the ERSST.v3 dataset used in this study was based on sparse observations in early years, an improved statistical method helped to make the dataset suitable for use in studying basin-wide features typical of ENSO and interdecadal variability.

4. Decadal changes in the relationship between the tropical Pacific and the North Pacific around late-1990s

As presented in the previous chapter, the most recent phase transition in the low-frequency variability mode occurred in 1998/99 from warm phase to cold phase. In association with this phase transition, it is identified that the ENSO occurred in 1990s and in 2000s have significantly different characteristics. In the present chapter, therefore, the differences of the Pacific climate variability before and after 1998/99 are investigated. In particular, the primary focus of this chapter is to demonstrate the distinguishable changes in the relationship between the tropical Pacific and the North Pacific since 1998/99.

4.1. CSEOF modes of the SSTA over the tropical Pacific and the North Pacific

The dominant modes of the SSTA over the tropical Pacific and the North Pacific during the 31-year period (1980-2010) were calculated using CSEOF analysis. Figure 4.1 illustrates the first CSEOF mode of the tropical Pacific SSTA (100°E-80°W, 30°S-20°N), which explains approximately 47% of the total variance. The spatial patterns of the first CSEOF mode for the tropical Pacific SSTA are characterized by strong positive SST anomalies in

the central and eastern tropical Pacific, resembling a typical El Niño event. The PC time series (the solid line in Fig. 4.3) is highly correlated ($r = 0.85$) with the Nino3 index (data not shown). Hence, the first CSEOF mode of the tropical Pacific SSTA appears to represent the dominant variability of the ENSO.

CSEOF analysis was also conducted for the North Pacific SSTA (100°E-80°W, 20°-60°N); the first mode explains approximately 24% of the total variability (Fig. 4.2). The spatial patterns of the first CSEOF for the North Pacific SSTA show negative anomalies with elliptical shapes over the western to central Pacific and positive anomalies along the eastern North Pacific. The patterns in Fig. 4.2 are similar to the structure of the PDO, which was first discussed by Mantua et al. (1997). To confirm this similarity, the correlation between the Mantua's PDO index and the first PC time series of the North Pacific SSTA (the dashed line in Fig 4.3) is calculated. The two time series are significantly correlated at 0.73. A difference, however, is observed between the CSEOF patterns and the PDO pattern. The CSEOF patterns are characterized by stronger meridional gradient of SSTA approximately along 40°N compared to the PDO structure. In this respect, the CSEOF patterns are comparable to the SSTA pattern of NPGO (Di Lorenzo et al. 2008, 2010), which represents decadal dynamics in the North

Pacific. Indeed, the NPGO index (available online at <http://www.o3d.org/npgo>.) and the first PC time series of the North Pacific SSTA are significantly correlated at -0.63. Thus, the SSTA patterns in the North Pacific reflect both the PDO and the NPGO features, which are dominant decadal variability in the North Pacific.

The PC time series of the first CSEOF of the tropical Pacific SSTA (solid line) and that of the North Pacific SSTA (dashed line) are presented in Fig. 4.3. The two PC time series are correlated at 0.47 from 1980 to 2010. However, there exists a marked difference in the relationship between the two PC time series before and after the late 1990s. The two PC time series are significantly correlated with each other in the most recent decade, but such a close relationship is obscure before the late 1990s; the correlation coefficient between the two PC time series is only 0.28 for the period 1980-1998, but the correlation coefficient is 0.83 for the period 1999-2010. This result suggests that the physical relationship between the dominant SSTA modes over the tropical Pacific and the North Pacific experienced an abrupt change occurring approximately in late 1990s. Thus, 1998/1999 was chosen as the inflection point in the large-scale physical relationship between the tropical Pacific and the North Pacific. For convenience, the period 1980-

1998 (19 years) is hereinafter referred to as the first period and the period 1999-2010 (12 years) is the second period.

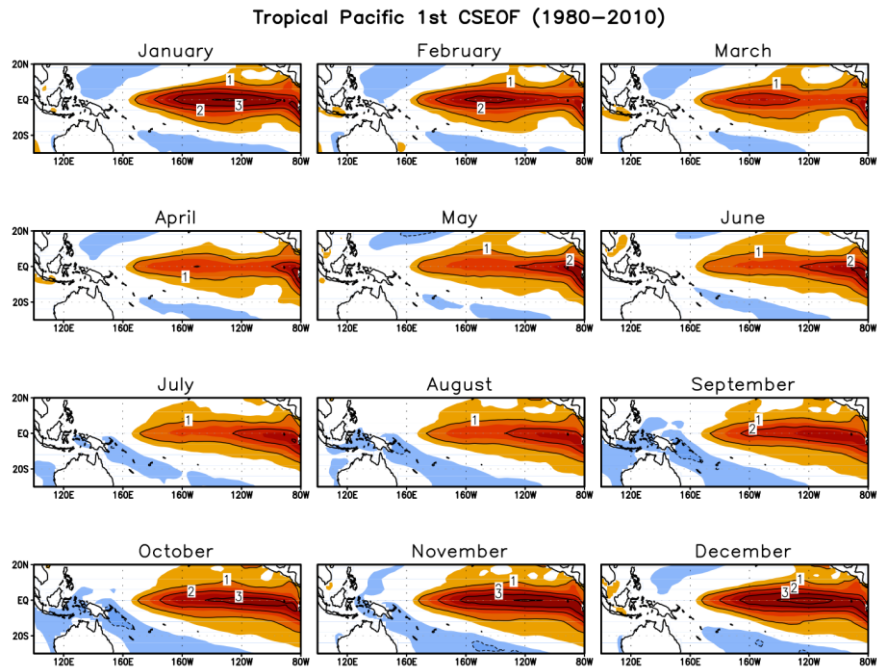


Fig.4.1. The first CSEOF loading vector of the 31-year (1980-2010) monthly SST anomalies over the tropical Pacific (100°E-80°W, 30°S-20°N).

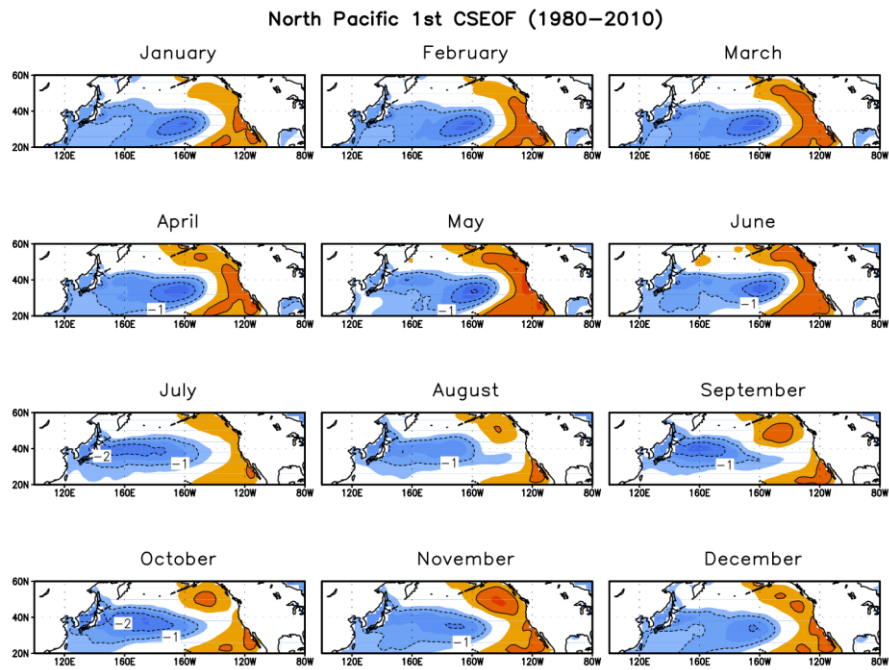


Fig.4.2. The first CSEOF loading vector of the 31-year (1980-2010) monthly SST anomalies over the North Pacific (100°E - 80°W , 20°N - 60°N).

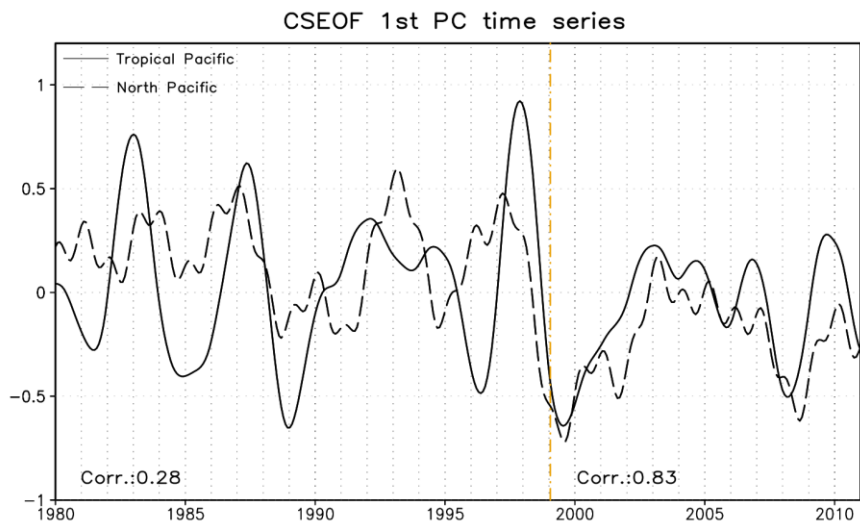


Fig.4.3 The first CSEOF PC time series of the tropical Pacific SST anomaly (solid line, corresponding to the loading vector in Fig. 4.1) and North Pacific SST anomaly (dashed line, corresponding to the loading vector in Fig. 4.2). The vertical dashed line indicates the year 1999.

4.2. Changes in the relationship between the tropical Pacific and the North Pacific

a. SST field

Figures 4.4 and 4.5 depict the first CSEOF mode of the SSTA in the tropical Pacific (10°S–20°N) and the regressed SSTA in the North Pacific (20°–60°N) for the first and second periods, respectively. The regressed North Pacific SSTA has R^2 values of 0.88 and 0.95 for the first and second period, respectively; the R^2 values measure the degree of fitting. Therefore, these figures represent the North Pacific SST anomalies evolving with the first CSEOF mode of the tropical Pacific SSTA. Because the monthly spatial patterns do not change significantly, seasonal mean SSTA patterns are presented in Figs. 4.4 and 4.5. A comparison between Fig. 4.4 and 4.5 reveals several remarkable differences between the two periods in terms of the relationship between the tropical Pacific and the North Pacific.

First, the ENSO feature captured by the first CSEOF mode of the tropical Pacific SSTA differs for the two periods; the first CSEOF mode of the tropical SSTA explains approximately 51.6% and 47.6% of the total variance for the first and the second periods, respectively. In the first period, the tropical warming features the conventional El Niño with an SSTA center located in the eastern Pacific for the entire year (Fig. 4.4). Unlike the first

period, the SSTA is stronger in the equatorial central Pacific, particularly for the spring and the summer seasons (March to August) in the second period (Fig. 4.5). Note that the tropical Pacific CSEOF patterns for the second period and the CP El Niño share some degree of similarity. Since CSEOF loading vectors are periodic functions, they repeat themselves perpetually. Therefore, physical evolution of the El Niño events presented in Figs. 4.4 and 4.5 may not necessarily be in time order; in order to understand the time sequence of the physical evolutions in Figs. 4.4 and 4.5, composite analysis was conducted for the reconstructed SSTA based on the first CSEOF mode. In the first period, 1982/1983, 1986/1987 and 1997/1998 are selected as the El Niño years according to the PC time series and 2002/2003, 2004/2005 and 2009/2010 are selected in the second period. As illustrated in Fig. 4.6, the amplitude of the evolution in the first period is comparable in autumn and winter and decreases gradually in the following year. SSTA in the second period also exhibits comparable magnitude in autumn and winter, but rapidly decays in the following year. Central Pacific warming is evident in the spring following a major El Niño event.

Second, a comparison of Figs. 4.4 and 4.5 reveals that the SSTA features over the North Pacific during a tropical warming event differ significantly in the two periods. In the first period, the regressed North

Pacific SSTA has the same sign in the eastern and the western North Pacific but has an opposite sign in the central North Pacific (Fig. 4.4). This zonal tripolar SSTA pattern is particularly evident during winter and spring. The regressed North Pacific SSTA patterns replicate the patterns in previous studies (Alexander et al. 2002; Deser and Blackmon 1995; Lau and Nath 1996; Zhang et al. 1996), which focused on the elucidation of the “atmospheric bridge mechanism”. In particular, the patterns in winter and spring are virtually identical to that presented in Figure 1 of Deser and Blackmon (1995), which was obtained from an EOF analysis for the period 1950-1992. In the second period, however, the regressed North Pacific SSTA is characterized by a positive SSTA extending from the northeastern Pacific to the tropical central Pacific and a negative SSTA over the western to central North Pacific that is slightly tilted in the southwest-northeast direction (Fig. 4.5). The positive SSTA extending southwestward from the western shore of North America to the tropical central Pacific is particularly clear during spring and summer (March to August). A major difference is that the SSTA in the eastern North Pacific extends further toward the equator in the second period than in the first period. It is also noteworthy that the positive SSTA in the eastern North Pacific extends across the Pacific to the western Bering Sea and the Sea of Okhotsk in the far-western North

Pacific. This SSTA pattern bears a strong resemblance to that of the NPGO variability (Di Lorenzo et al. 2010). This result agrees with previous studies that the amplitude of the NPGO-related SSTA patterns are larger than that of the PDO pattern during the last decade (Bond et al. 2003; Di Lorenzo et al. 2008). In particular, Di Lorenzo et al. (2010) expounded a dynamical link between the NPGO and the CP El Niño; both climate patterns are well known for their increasing occurrence frequencies in the recent decade. A comparison of Figs. 4.4 and 4.5 suggests that the physical connection between the tropical Pacific SSTA variability and the associated North Pacific SSTA variability experienced a significant change since approximately 1998/1999 and that the principal mechanism linking the tropical Pacific and the North Pacific may have changed in the late 1990s.

**Tropical Pacific CSEOF 1st mode (10S–20N)
& Regressed North Pacific SST (20N–60N) : 1980–1998**

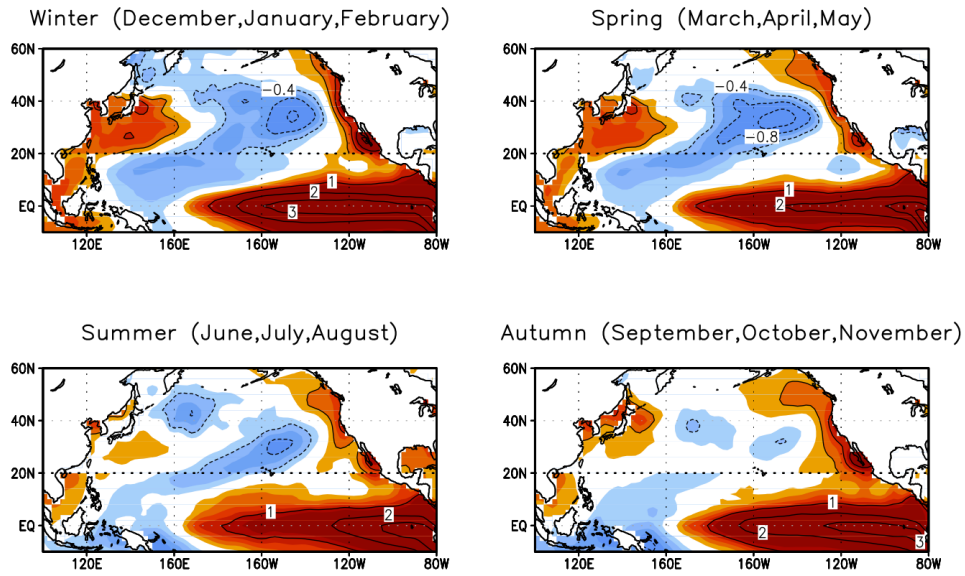


Fig.4.4. The first CSEOF loading vector of the tropical Pacific (100°E–80°W, 30°S–20°N) SST anomaly during the period 1980–1998. The North Pacific (100°E–80°W, 20°N–60°N) region depicts the regression of the SST anomaly onto the first CSEOF loading vector in the tropical Pacific. Each panel represents the seasonal mean spatial pattern.

**Tropical Pacific CSEOF 1st mode (10S–20N)
& Regressed North Pacific SST (20N–60N) : 1999–2010**

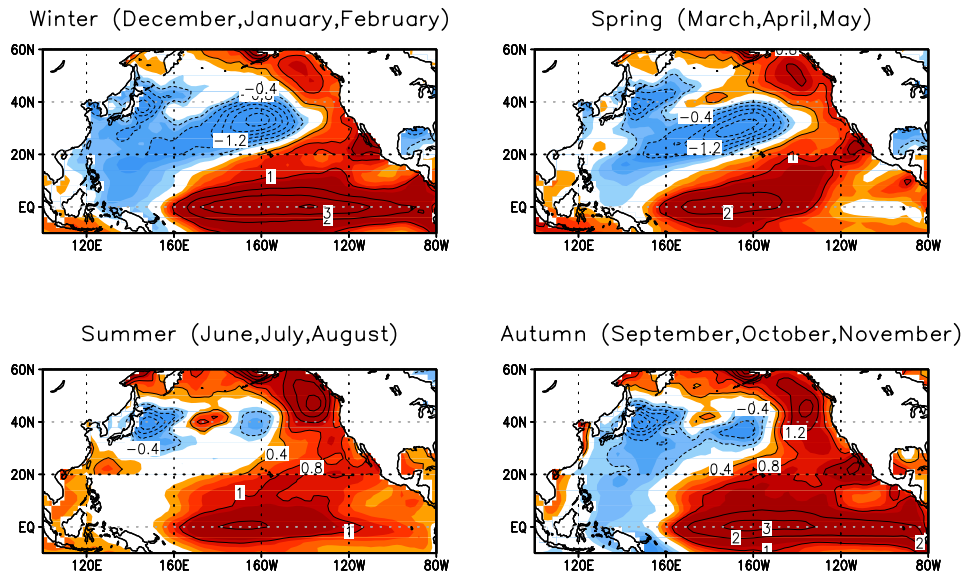


Fig.4.5. The same map as in Fig. 4.4 but for the period 1999-2010.

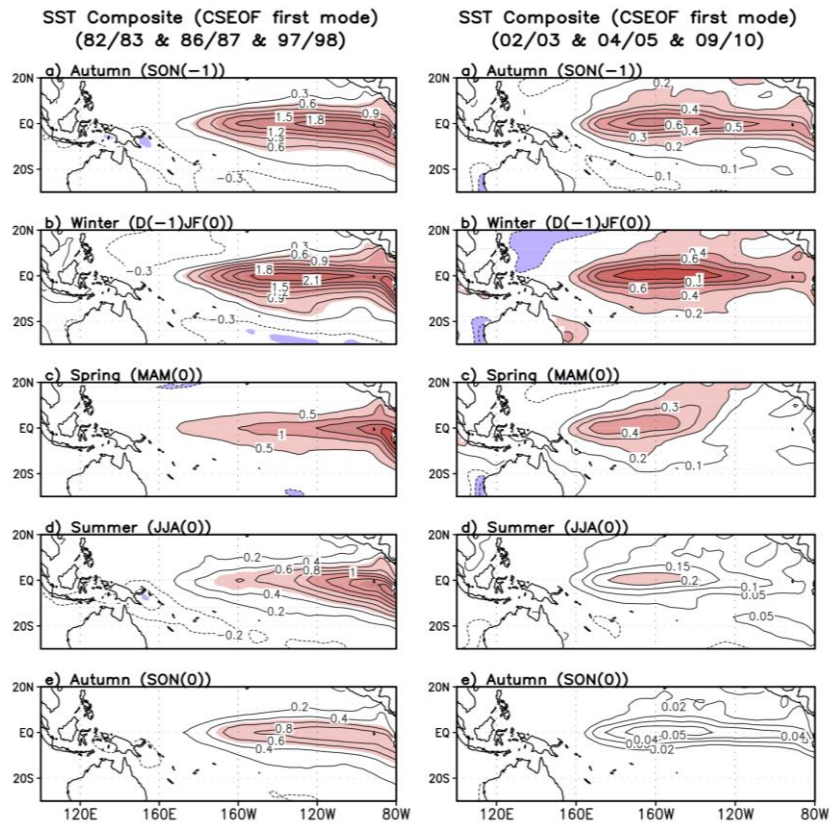


Fig.4.6. Composite map of the reconstructed first CSEOF loading vectors of the tropical Pacific SSTA. Left panel shows composite of El Niño years in the first period (1982/1983, 1986/1987 and 1997/1998) and right panel shows that of the second period (2002/2003, 2004/2005 and 2009/2010).

b. Surface fields

To understand the detailed changes in the physical relationship between the tropical Pacific and the North Pacific, the atmospheric variability associated with the first CSEOF mode of the tropical Pacific SSTA was examined for the first and second periods. Figure 4.7 displays the regressed spatial patterns of the SSTA over the North Pacific (20° – 60° N, shading) and the 1000-hPa geopotential height anomaly over the Pacific basin (10° S– 70° N, contour) with the leading CSEOF mode of the SSTA over the tropical Pacific (10° S– 20° N, shading) for the first period. The R^2 values of the 1000-hPa geopotential height field is 0.82. The seasonal means for winter (January-February), spring (March-May), and summer (June-August) are shown in Fig. 4.7; the seasons were divided based on similarities in the evolution patterns of the physical variables.

As illustrated in Fig. 4.7a, the ENSO is associated with an intensification and eastward shift of the Aleutian Low as evidenced by a significant negative geopotential height anomaly and a weaker anomaly of the opposite polarity over the northeastern Canada and the subtropical western Pacific during winter in the first period. The overall features of the ENSO-related atmospheric anomaly patterns for the first period closely resemble the so-called Pacific/North America (PNA) teleconnection pattern

(Wallace and Gutzler 1981). Many studies have indicated that ENSO serves as a strong tropical heat source, which in turn produces a Rossby wave response emanating into the extratropics, particularly the PNA region (Horel and Wallace 1981; Hoskins and Karoly 1981; Simmons et al. 1983). It has also been suggested that the ENSO-related atmospheric circulation over the PNA region functions as a “bridge” whereby the tropical SST anomalies associated with the ENSO induce strong SST anomalies in the extratropical North Pacific.

To further examine the physical relationship of the tropical Pacific and the North Pacific in the first period, the regressed net surface heat flux (the sum of latent heat, sensible heat, and shortwave and longwave radiative fluxes) and wind at 1000 hPa are investigated; the R^2 values are 0.92 and 0.94 for 1000-hPa wind and net surface heat flux, respectively. The resulting patterns are presented in Fig. 4.8. Positive fluxes are directed from the ocean to the atmosphere. In accordance with the intensified Aleutian Low, the net surface heat flux shows a relatively strong response in winter. As shown in Fig. 4.8a, the northerly wind anomaly advects cold and dry air from high latitudes to the central North Pacific, leading to a positive net surface heat flux anomaly (i.e., a flux from the ocean to the atmosphere) and subsequently producing a negative SSTA. The southerly wind anomaly, in

contrast, advects warm and moist air along the western coast of North America, resulting in a negative net surface heat flux anomaly and positive SSTA. Additionally, the anomalous westerly wind on the southern flank of the Aleutian Low strengthens the climatological westerly flow. The increased local wind speed results in the cooling of the ocean mixed layer through an upward surface heat flux anomaly and ocean vertical mixing. The surface heat flux and the surface wind anomalies are consistent with the SSTA over the North Pacific (Figs. 4.7 and 4.8). These results indicate that the El Niño-related atmospheric circulation anomalies over the middle latitudes induce a major SSTA pattern over the North Pacific via air-sea interaction in the first period, and this connection is associated with the “atmospheric bridge mechanism” in which the tropical Pacific SSTA forces the SSTA in the North Pacific.

1980–1998 SST & 1000hPa GPH

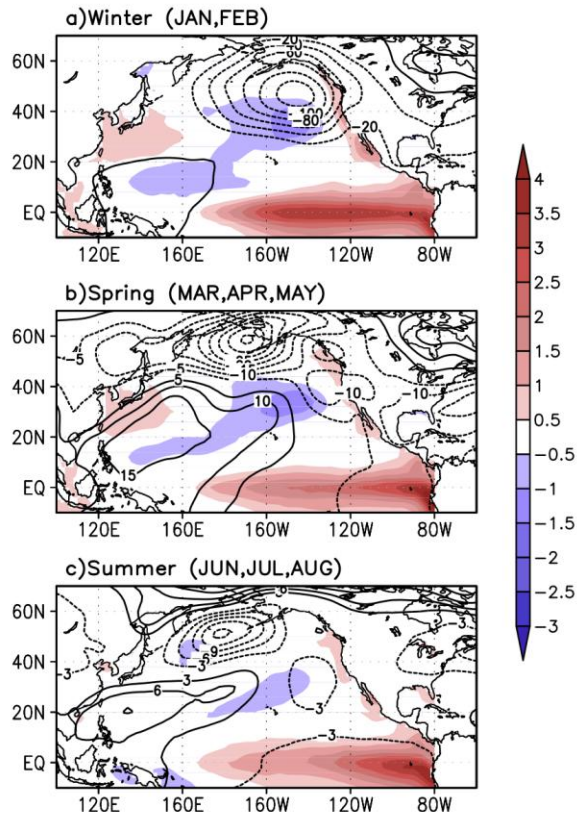


Fig.4.7. The first CEOF loading vector of the tropical Pacific (100°E-80°W, 10°S-20°N) SST anomaly (shaded) for (a) winter (January and February), (b) spring (March to May), and (c) summer (June to August) during the period of 1980 to 1998. The 1000-hPa geopotential height anomaly (100°E-60°W, 10°S-70°N, contour) and the North Pacific SST anomaly (100°E-80°W, 20°N-60°N, shading) are obtained from a regression analysis onto the first CEOF loading vector of the tropical Pacific SST anomaly.

1980–1998 Net Heat Flux & 1000hPa Wind

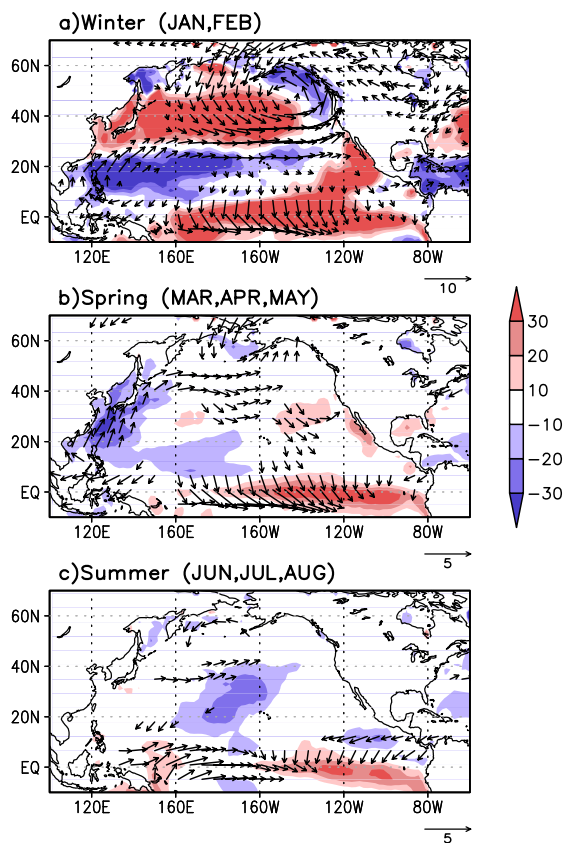


Fig.4.8. A regression map of the 1000-hPa wind anomaly (vector) and net surface heat flux anomaly (shaded) for a) winter, b) spring and c) summer corresponding to the first CSEOF loading vector of tropical Pacific SST during the period 1980-1998. Note that the vector scale is different for each panel.

The characteristics of the relationship between the tropical Pacific and the North Pacific in the second period (1999–2010) are examined in Fig. 4.9. Here, the regressed 1000-hPa geopotential height field has an R^2 value of 0.90. The extra-tropical atmospheric responses to warming in the tropical Pacific for the second period are distinctively different from those in the first period (Fig. 4.7). One major difference between Figs. 4.7 and 4.9 is observed in the atmospheric evolution patterns from winter to summer. In the first period, negative anomaly patterns in the 1000-hPa geopotential height dwell in the North Pacific for several seasons, with positive geopotential height anomaly patterns over the subtropical western North Pacific (Fig. 4.7). In the second period, in contrast, the 1000-hPa geopotential height anomaly displays a significant season-to-season variation (Fig. 4.9). This difference between the first and the second periods reveals an interesting feature in the winter season. An important feature of the 1000-hPa geopotential height pattern associated with the warming in the tropical Pacific is anomalous Aleutian Low centered at 35°-40°N, with positive pressure anomaly in the higher-latitude Pacific (50°-70°N). This atmospheric pattern and the NPO pattern share a common feature—a southward shift of the atmospheric action center in the winter season. The NPO-like pattern is a distinguishing feature of the second period from the

PNA-like pattern of the first period. Several studies have shown that the NPO-like mid-latitude atmospheric variability can influence tropical ENSO-like variability (Barnett et al. 1999; Pierce et al. 2000; Vimont et al. 2003a). In particular, the “seasonal footprinting mechanism” suggested by Vimont et al. (2001) explains the process of the boreal winter NPO pattern driving the warm SST anomaly in the tropical central Pacific by the end of spring/summer through an air-sea interaction, as evidenced by the net surface heat flux anomaly. This mechanism offers a plausible explanation for how the atmospheric variability in the subtropical Pacific associated with the NPO results in oceanic variability in the tropical Pacific; the wind-evaporation-SST feedback is suggested as a potential air-sea coupling mechanism (Xie and Philander 1994).

To investigate the mechanistic details of the connection between the tropical Pacific and the North Pacific in the second period, the regressed 1000-hPa wind and net surface heat flux for the second period were examined (Fig. 4. 10). The R^2 values are 0.98 and 0.97 for wind and net surface heat flux, respectively, indicating that the regression fitting is nearly perfect. The spatial pattern of the surface wind field associated with the NPO-like atmospheric variability in winter is characterized by a southward shift of the action center in comparison with the first period (see Figs. 4.8a

and 4.10a). Therefore, the atmospheric variability in the North Pacific may be more closely linked to the subtropical region in the second period. The southeasterly anomaly off the west coast of North America occupies a wider area of the eastern North Pacific than in the first period; this pattern appears to be consistent with the increased downward heat flux off the coast of North America via the advection of warm and moist air. The increased downward heat flux together with the increased Ekman transport toward the continent results in positive SST anomalies in the eastern North Pacific. The positive SSTA, therefore, covers a wider area than in the first period (Fig. 4.9a). Conversely, the northwesterly anomaly over the central Pacific advects cold, dry air, leading to increased upward heat flux and a negative SST anomaly. The southern flank of the anomalous Aleutian Low extends further toward the equator than in the first period and is located in the subtropical region at approximately 20°N; note that the southern edge of the anomalous Aleutian Low is located north of 30°N in the first period (Fig. 4.8a). Because the atmospheric variability associated with the ENSO is characterized by an equatorward shift of the action center, it is speculated that the North Pacific atmospheric variability potentially excites a sequence of variation in the subtropical and the tropical regions. In particular, the air-sea interaction associated with the southerly wind anomaly in the

southeastern quarter of the anomalous Aleutian Low is responsible for producing a positive SSTA extending from the Northeastern Pacific to the tropical central Pacific.

The most striking feature of Fig. 4.10 is found in the spring season. As shown in Fig. 4.10b, the center of the anomalous westerly wind over the tropical Pacific is located in the vicinity of 180° - 160° W in the second period, whereas the westerly anomaly is located further to the east in the first period, in the vicinity of 140° - 120° W (Fig. 4.8b). The different locations of the westerly wind anomaly over the tropical Pacific in the two periods characterize the different types of tropical warming events, as illustrated in Figs. 4.7b and 4.9b. The westerly wind anomaly, which opposes the prevailing trade winds, leads to a reduced wind speed and subsequently reduces evaporation and oceanic turbulent mixing, thereby warming the underlying ocean. In the first period, the warming event shows stronger SST anomalies in the eastern Pacific, whereas the second period shows the maximum SST anomalies in the central Pacific. Most notably, the northerly wind anomalies over the North Pacific in spring extend into the subtropical and the tropical Pacific, creating an atmospheric connection between the middle latitudes and the tropical Pacific. The related tropical Pacific westerly anomalies are located in the equatorial western and central Pacific

and thus are responsible for changing the ensuing El Niño characteristic into a CP-type El Niño. Therefore, it can be inferred from Fig. 4.10 that the mid-latitude atmospheric variability may have affected the tropical ENSO characteristics.

It should be emphasized, however, that the mid-latitude atmospheric variability cannot fully explain a generation of the CP-type El Niño in the second period. Note that the wintertime NPO pattern appears concurrently with an El Niño event (Fig. 4.9a); thus, the CP-type El Niño is not necessarily induced by the mid-latitude NPO forcing. Nonetheless, it is clear that the mid-latitude atmospheric variability in the second period is more strongly connected with the subtropical and the tropical Pacific than in the first period. The mid-latitude atmospheric variability appears to favor a CP-type El Niño from winter to summer. Specific dynamics of the CP-type El Niño has yet to be fully revealed, but many recent studies on the CP-type El Niño agree on the importance of the mid-latitude atmospheric forcing for the development of the CP-type El Niño (Di Lorenzo et al. 2010; Furtado et al. 2012; Kim et al. 2012; Yu et al. 2010; Yu and Kim 2011); results in this study are consistent with these studies.

1999–2010 SST & 1000hPa GPH

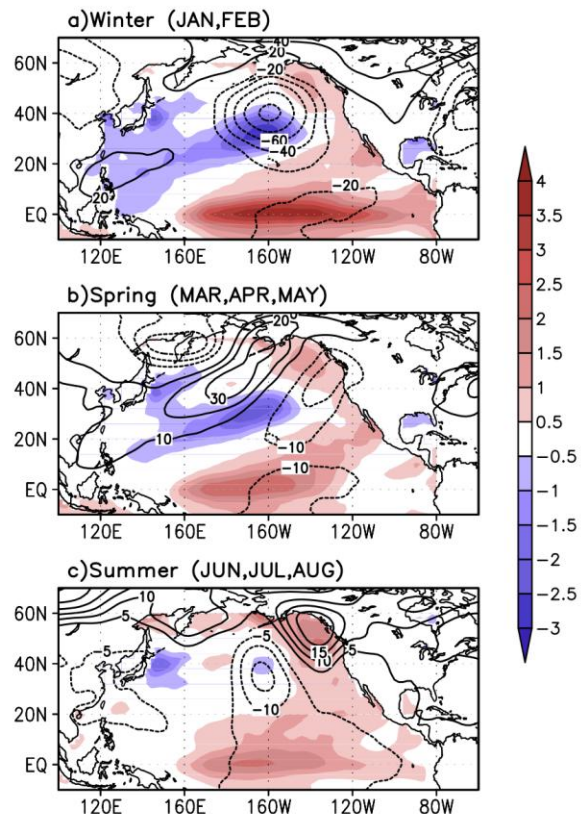


Fig.4.9. The same map as in Fig. 4.7 but for the period 1999-2010.

1999–2010 Net Heat Flux & 1000hPa Wind

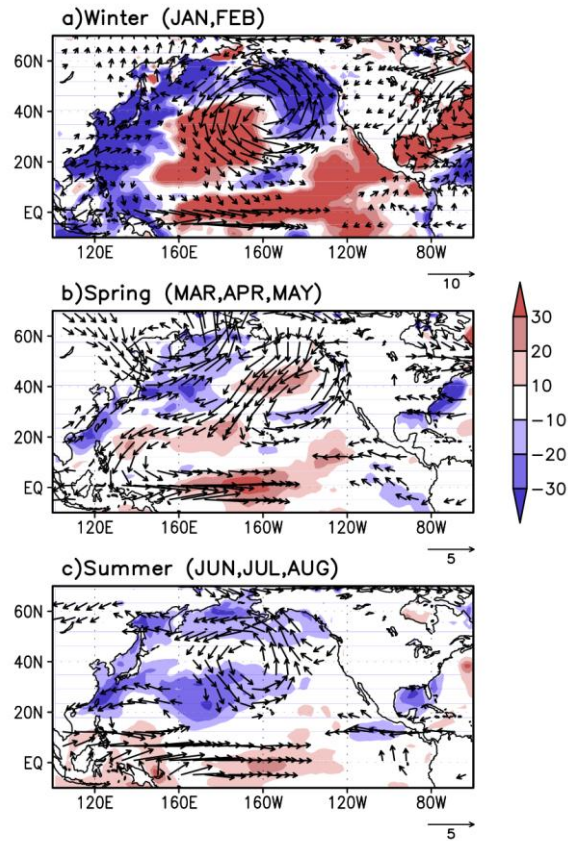


Fig.4.10. The same map as in Fig. 4.8 but for the period 1999-2010.

c. Vertical circulation fields

To investigate the detailed physical relationship between the tropical Pacific and the North Pacific, the zonal mean (150° - 170° W) vertical cross-section of the regressed geopotential height and wind fields (meridional component and omega velocity) were plotted for the first period, and the results are presented in Fig. 4.11. Because the meridional band at 150° - 170° W represents a central location of action in the North Pacific (Figs. 4.7 and 4.11), this region is selected for further investigation. The vertical structure of the negative geopotential height anomalies in the high-latitude region in Fig. 4.11 represents an equivalent barotropic structure of the Aleutian Low. In the tropics and the subtropics, in contrast, significant positive geopotential height anomalies appear only in the middle-to-upper troposphere. The regressed zonal-mean vertical structure of the wind indicates a distinct El Niño-induced anomalous Hadley circulation, which exhibits an enhanced ascending motion in the equatorial region and a descending counterpart in the subtropics and the middle latitudes up to approximately 30° N (Fig. 4.11a). This structure is persistent until spring, although the magnitude of the circulation weakens (Fig. 4.11b). As presented in Fig. 4.7, the warm SST anomaly in the equatorial Pacific decreases in magnitude from winter to summer, which is consistent with

the magnitude of the El Niño-induced vertical circulation decrease during the same time interval (Fig. 4.11). As illustrated in Figs 4.7, 4.8 and 4.11, the above results suggest that the variability initiated in the tropical ENSO exerts a significant influence on the North Pacific via both the ocean and the atmosphere. Previous studies on the “atmospheric bridge mechanism” support this explanation.

Figure 4.12 shows the anomalous zonal-mean (150° - 170° W) vertical circulation pattern for the second period. A striking difference between Figs. 4.11 and 4.12 is revealed over the middle-to-high latitudes. In accordance with the NPO-like surface pressure field in the winter of the second period (Fig. 4.9a), the vertical circulation field is characterized by patterns of opposite signs to the north and south of 50° N; an equivalent barotropic positive pressure anomaly with a descending motion is clearly evident at 60° - 70° N, and a negative pressure anomaly with an ascending motion is apparent at 30° - 50° N (Fig. 4.12a). There is also a striking difference between the two periods in the El Niño-related vertical circulation patterns over the tropics and the subtropics. The anomalous descending motion accompanying the ascending motion over the equator induced by El Niño appears to be confined to the area south of approximately 15° N; note that the downward branch of the anomalous Hadley cell in the first period

extends to approximately 30°N (Fig. 4.11a). The structure of the vertical circulation shows that El Niño does not exert a significant influence on the North Pacific in the second period as a comparison between Figs. 4.11 and 4.12 shows. In spring, there is a remarkable difference in circulation in the mid-latitude. Fig. 4.12b shows that the enhanced descending motion over the mid-latitudes (approximately 30° – 40°N) is closely related to the ascending motion in the subtropics (approximately 10° – 20°N); this pattern is characterized by a southward shift of the mid-latitude atmospheric circulation and suggests that the mid-latitude atmospheric variability has a potential to influence on the subtropical and tropical Pacific Ocean. This physical change appears to be related to the change in El Niño characteristics into the CP-type El Niño through the wind-SST coupling mechanism (Xie and Philander 1994) in the second period (see also Fig. 4.9b). It is necessary to conduct idealized model experiments, however, to identify the cause-and-effect relationship between the changes in the mid-latitude circulation and the CP-type El Niño, which is beyond the scope of this study.

The analyses presented in this chapter suggest that the interaction between the mid-latitude atmospheric variability and the El Niño variations in the second period is clearly distinguishable from that in the first period.

The dominant mode of the tropical Pacific SSTA variability is characterized by the CP-type El Niño in the second period, which is consistent with the increased frequency of CP El Niño events in the recent decade (Kug et al. 2009; Lee and McPhaden 2010; Yeh et al. 2009). Thus, the altered connection between the tropical Pacific and the North Pacific may have been responsible for the recent changes in the characteristics of El Niño. One may argue that the two largest El Niño events in 1982-1983 and 1997-1998 can induce a decadal change in the relationship between the tropical Pacific and the North Pacific after 1999. To examine this argument, CSEOF and regression analyses were conducted without the two major El Niño events for the first period. Similar results to those in Fig. 4.4 were obtained (data not shown).

Lat.-Pres.(190E-210E),1980-1998

GPH & Vwind & Omega

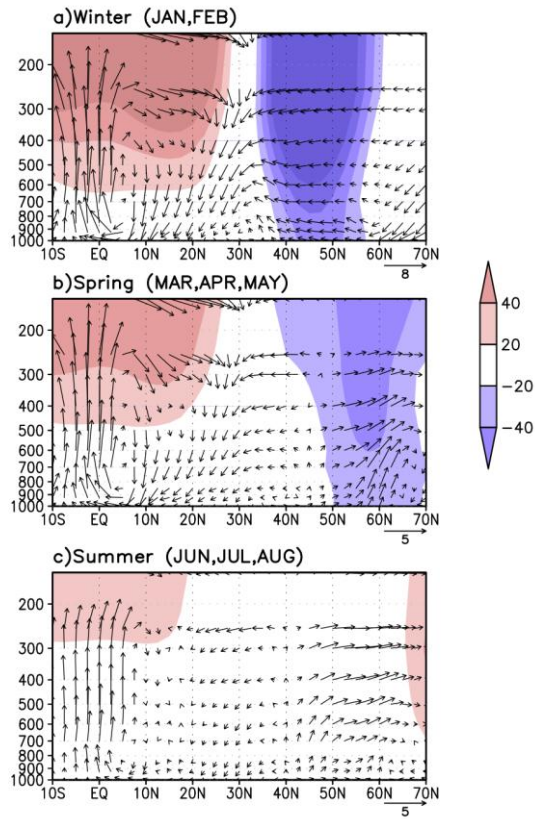


Fig.4.11. A regression map of the vertical cross-section for the latitude-height geopotential height (shaded) and wind (vector) field averaged over the longitude band from 150° to 170°W for a) winter, b) spring and c) summer corresponding to the first CSEOF loading vector of tropical Pacific SST during the period 1980-1998.

Lat.-Pres.(190E-210E),1999-2010

GPH & Vwind & Omega

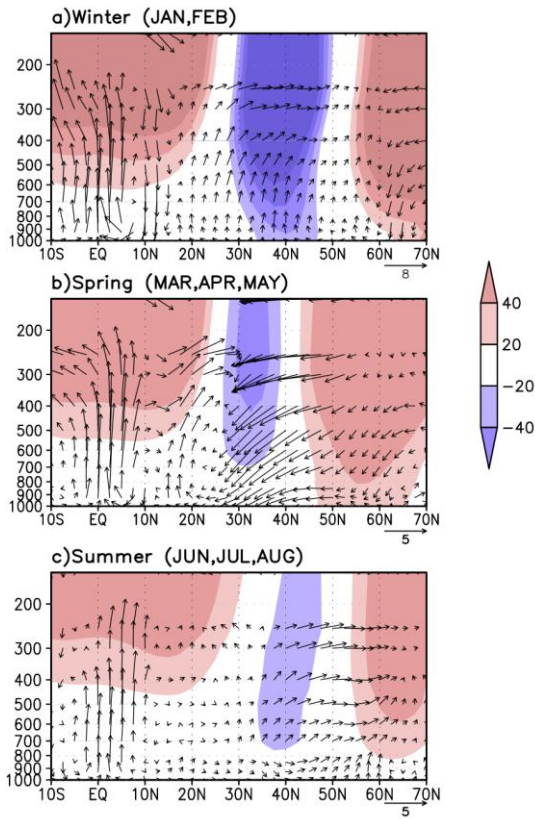


Fig.4.12. The same map as in Fig. 4.11 but for the period 1999-2010.

5. Relationship between the climate variability in the Bering Sea and large-scale circulation in the Pacific during 1999-2010

It is pointed out in the previous chapter that the interaction between the tropical Pacific and the North Pacific in the period 1999-2010 is distinguishable that in the period 1980-1998. The cause of decadal change in the relationship between the tropical Pacific and the North Pacific was not discussed in detail in the previous chapter. This transition is possibly one aspect of internal atmosphere-ocean fluctuation on a decadal time scale in association with the low-frequency phase transition occurred in 1998/99. In addition to the contribution of the phase transition in low-frequency variability, the intensified global warming signal in 2000s also seems to be responsible for the climate change suggested in chapter 4. Indeed, Sea ice concentration in the Arctic Ocean exhibits a strong melting trend in the late 1990s (Comiso et al. 2008), and high-latitude (50° – 90° N) surface air temperature also shows a strong warming trend during the same period (data not shown). It is noteworthy that the change in the physical relationship between the tropical Pacific and the North Pacific coincides with these conspicuous global warming signals. In this chapter, therefore, the influence of the global warming signal represented by the recent

warming in the sub-arctic Pacific Ocean on the climate variability over the Pacific are investigated.

5.1. Recent warming in the Bering Sea and its relationship to the North Pacific Oscillation

a. Changes in the relationship between the Bering Sea and the North Pacific

The Bering Sea, a northern extension of the North Pacific Ocean, is located between Russia and Alaska and is the third largest semi-enclosed sea in the world. The Bering Sea is connected to the Chukchi Sea, which is a marginal sea of the Arctic Ocean, through the Bering Strait. In a global sense, the Bering Sea acts as the Pacific gateway, through which the North Pacific and the Arctic Ocean exchange heat and water. The Bering Sea is one of the most productive marine resources in the world and provides nearly half of the US fisheries production (National Research Council, 1996). For this reason, many oceanographers have tried to understand the variability of the marine ecosystem in the Bering Sea. In particular, its relationship with climate variability has long been the focus of attention (Grebmeier et al. 2006; Overland and Stabeno 2004; Hunt et al. 2002; Kruse 1998; Brodeur et al. 1999). Furthermore, the Bering Sea, as a marginal section of the North Pacific Ocean, is sensitive to Pacific large-scale climate phenomena such as

the ENSO (Niebauer 1998) and the PDO (Hare and Mantua 2000; Overland et al. 1999). Understanding the oceanic and atmospheric variability over the Bering Sea, therefore, is essential from both ecological and climatological perspectives.

Atmospheric and oceanic parameters in the Bering Sea vary over a wide range of time scales, from interannual to multi-decadal scales, including trends or climate regime shifts. In particular, recent studies have noted that noteworthy changes in the Bering Sea have occurred recently. For example, the Bering Sea experienced marked warming and a reduction in sea ice during the last decade (Grebmeier et al. 2006; Hunt et al. 2002; Overland and Stabeno 2004; Stabeno et al. 2007). In particular, the striking warming events were concentrated in the years 2000-2005 (Overland et al. 2012). Prominent anomalies in atmospheric and oceanic conditions in the Bering Sea occurred during 1997 and 1998. The SST in the Bering Sea increased up to 5°-6°C above the average for August and September in 1997, and SST continued to be approximately 2°C higher than average through the summer of 1998. The biological conditions were also anomalous, including major coccolithophorid blooms, salmon returns far below predicted numbers, and the unusual presence of whales over the middle shelf (Hunt et al. 1999; Kruse 1998; Minobe 2002; Napp and Hunt 2001; Schumacher et al. 2003;

Stabeno et al. 2001; Stockwell et al. 2001). It is likely that these changes in the Bering Sea are closely related to the state of the North Pacific climate system. Moreover, Minobe (2002) argued that the changes in the Bering Sea in the late-1990s are a part of the Pacific-scale atmospheric and oceanic change, which is regarded as a potential climatic regime shift. The linkage between the Bering Sea and the North Pacific large-scale climate variability was supposed to be established primarily through the atmosphere; in particular, the connection between the two regions seems to vary according to the strength and position of the Aleutian Low (Niebauer 1988; Overland et al. 1999; Stabeno et al. 2001).

Meanwhile, the large-scale climate variability in the North Pacific also seems to have undergone a significant change during the last decade. According to recent studies, the amplitude of NPGO, which is characterized by a dipole-like SST pattern in the North Pacific became larger than the PDO amplitude during the recent decade (Bond et al. 2003; Di Lorenzo et al. 2008; Yeh et al. 2011). The NPGO appears to be driven by the atmospheric North Pacific Oscillation (NPO) (Rogers 1981), which is the second dominant mode of sea level pressure variability in the North Pacific (Ceballos et al. 2009; Di Lorenzo et al. 2010; Furtado et al. 2011). The NPO pattern consists of a

meridional dipole in sea level pressure, with centers of action on both sides of approximately 50°N.

As noted above, the climate in the Bering Sea and the North Pacific seems to have experienced remarkable changes in the recent decade. It is necessary to contemplate whether the changes in different parts of the Pacific are physically and dynamically linked with each other or not. In this section, therefore, it is identified that the pattern of the North Pacific variability that is associated with the major physical changes in the Bering Sea, focusing particularly on the recent decade (1999-2010).

Figure 5.1 illustrates the first CSEOF loading vector for the SST anomaly (SSTA) over the Bering and Chukchi Seas (160°E-160°W, 54°-76°N) during the 31-year period of 1980-2010, which explains approximately 31% of the total variance in SSTA in this region. Because the spatial patterns show a positive SSTA throughout the whole year, the seasonal (3-month) mean CSEOF loading patterns are presented in Fig. 5.1. The corresponding PC time series, presented as a black bar in Fig. 5.2, exhibits a weak warming trend from 1980 to 1997, with the warmest year in 1997 followed by a sharp cooling until 1998. This result agrees with previous studies, which documented extreme anomalous conditions in the Bering Sea during 1997 and 1998; the warmest temperature ever observed before appeared in 1997,

which is followed by rapid cooling until 1999 (Hunt et al. 1999; Kruse 1998; Minobe 2002; Napp and Hunt 2001; Schumacher et al. 2003; Stabeno et al. 2001; Stockwell et al. 2001). After an abrupt decline from 1998-1999, SST displayed a sharp increase from 1999 to 2003 and the summer of 2003 marked the warmest year in the entire record (1980-2010). This result is consistent with the recent studies suggesting warming in the Bering Sea in the early 2000s (Grebmeier et al. 2006; Hunt et al. 2002; Overland and Stabeno 2004; Overland et al. 2012; Stabeno et al. 2007). Although there is no warming trend since 2003, SST over the Bering Sea has been warmer during 2003-2010 compared with the mean SST in 1980-2010.

To identify any links between the Bering and Chukchi Seas and climate variability in the North Pacific, North Pacific (100°E-80°W, 20°-80°N) SSTA data were analyzed via CSEOF analysis. The seasonally (3-month) averaged loading vector of the first CSEOF is presented in Fig. 5.3; the first mode explains approximately 23% of the total variability. The corresponding PC time series is shown in Fig. 5.2 as a blue curve. The spatial patterns in Fig. 5.3 are similar to the structure of the PDO, which features negative SSTA with an elliptical shape over the western to central Pacific and positive SSTA along the eastern North Pacific. Correlation between the first PC time series of the North Pacific SSTA and the Mantua's PDO index is 0.73 confirming the

similarity between the first CSEOF (Fig. 5.3) and the PDO patterns. On the other hand, the strong meridional gradient of SSTA along approximately 40°N in Fig. 5.3 is more in line with the structure of the NPGO than the PDO. Indeed, the NPGO index and the first PC time series of the North Pacific SSTA are also significantly correlated at -0.63. In terms of the spatial pattern and the amplitude time series, the first CSEOF loading vector of the North Pacific SSTA (Fig. 5.3) reflects both the PDO and the NPGO features.

The PC time series of the first CSEOF of the SSTA in the Bering and Chukchi Seas (black bar) and that of the North Pacific (blue line) are presented in Fig. 5.2. One notable feature in Fig. 5.2 is the remarkable difference in the relationship between the two PC time series before and after 1999. The two PC time series are significantly correlated ($r = 0.74$) with each other in 1999-2010, but the correlation is obscure ($r = 0.04$) in 1980-1998. This result implies that the link between the Bering and Chukchi Seas and the North Pacific SST variability during the recent decade (1999-2010) is clearly distinguishable from that in the previous period (1980-1998). The Bering Sea appears to be more closely connected to the North Pacific in terms of SST variations after it experienced the unusual physical conditions during 1997-1998.

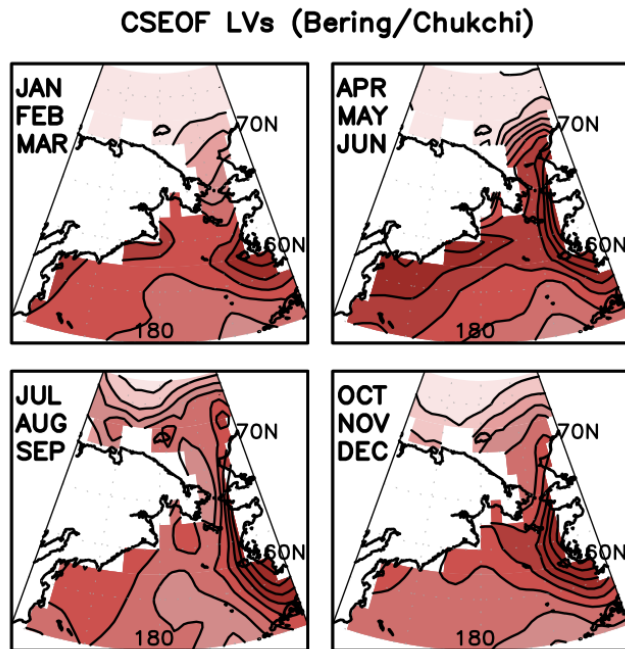


Fig.5.1. The first CSEOF loading vectors of the 31-year (1980-2010) monthly SSTA in the Bering and Chukchi Seas (160°E-160°W, 54°-76°N). Each spatial pattern represents the seasonal (3-month) average of the loading vectors.

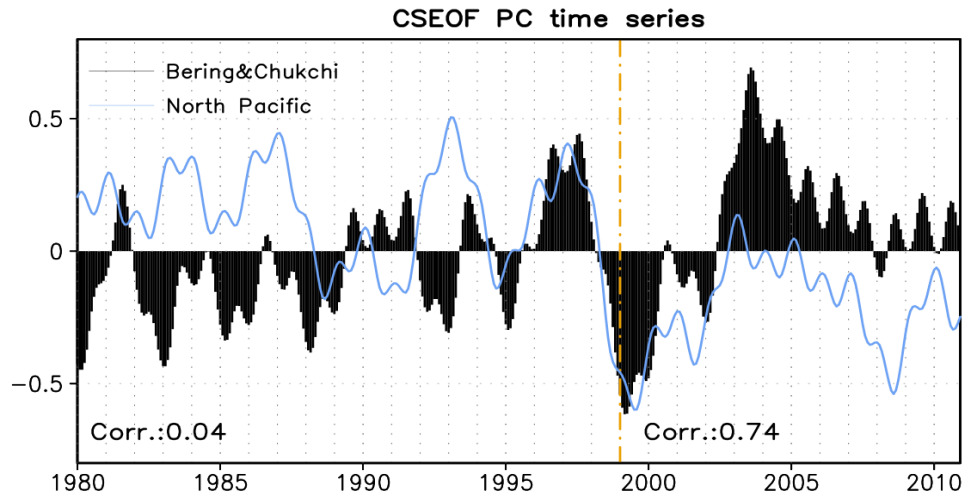


Fig.5.2. The CSEOF PC time series of the Bering and Chukchi SST anomaly (black bar, corresponding to the loading vectors in Fig. 5.1) and North Pacific SST anomaly (blue line, corresponding to the loading vector in Fig. 5.3). The vertical dashed line indicates the year 1999.

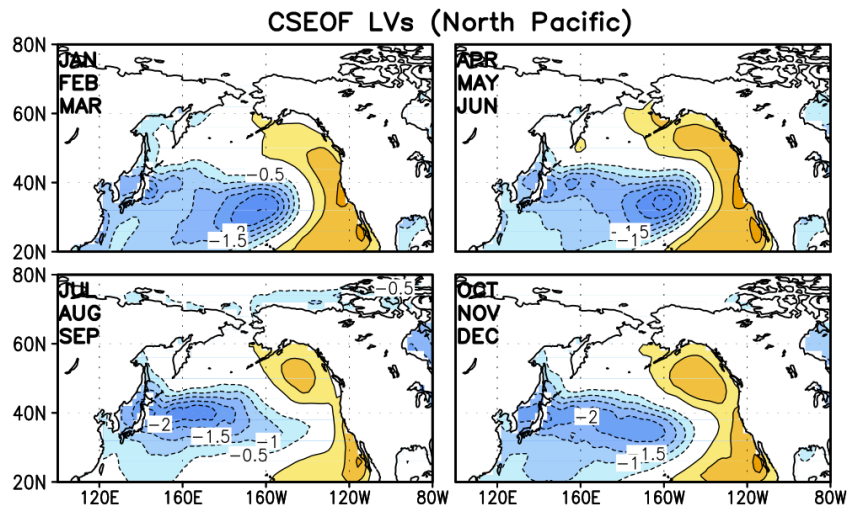


Fig.5.3. The first CSEOF loading vectors of the 31-year (1980-2010) monthly SSTa in the North Pacific (100°E-80°W, 20°-80°N). Each spatial pattern represents the seasonal (3-month) average of the loading vectors.

b. Atmospheric and oceanic variability in the Bering Sea during 1999-2010

Before the linkage between the Bering Sea and the North Pacific from 1999 to 2010 could be clarified, the variability of the physical environment over the Bering Sea during this period needed to be analyzed. Figure 5.4 shows the seasonal (3-month) mean patterns of the first CSEOF loading vector for the Bering and Chukchi SSTA from 1999 to 2010; the first mode explains approximately 38% of the total variability. The first CSEOF loading vector for the Bering and Chukchi SSTA from 1999 to 2010 is similar to that of the entire record (1980-2010) in Fig. 5.1, both showing a positive SSTA throughout the year. In particular, Fig. 5.4 displays large anomalies over the shallow shelf in the eastern Bering Sea. The corresponding PC time series exhibits almost the same variability as that of the entire period in Fig. 5.2 ($r = 0.95$). It should be pointed out that SSTA generally peaks in summer from July to September.

Variation of sea ice concentration is a crucial component of the physical environment in the Bering and Chukchi Seas that interacts with the ocean and the atmosphere primarily by altering the absorption of solar radiation and surface heat flux. Therefore, regression analysis was performed to identify the SIC and the net surface energy flux patterns over the Bering and Chukchi Seas, corresponding to the SSTA patterns in Fig. 5.4.

Figure 5.5 displays the regressed spatial patterns of the SIC anomaly (contour) and the net surface flux anomaly (shading) onto the first CSEOF mode of the Bering and Chukchi SSTA in 1999-2010. The R^2 values, which measure the goodness of regression fit, are higher than 0.95 for both the SIC and the net surface flux. Thus, the amplitude time series of the regressed patterns in Fig. 5.5 are essentially identical to that of the Bering and Chukchi SSTA in Fig. 5.4. The R^2 values, by contrast, are approximately 0.6 for the period of 1980-1998. These relatively small R^2 values indicate that a strong physical connection between the SSTA and the SIC or the net surface flux was not established in the Bering Sea in 1980-1998; thus, the following discussion focuses on the period from 1999 to 2010. The regressed SIC anomalies in Fig. 5.5 are generally negative throughout the year, suggesting a natural outcome that warmer SST results in smaller SIC. The Bering Sea is subjected to a large seasonal variation of insolation, which results in the pronounced seasonality of the sea ice cover. Beginning roughly in November, sea ice prevails in the northern Bering Sea and SIC reaches its maximum in March or early April. From spring to summer, with increased solar radiation and temperature, the Bering Sea is in virtually ice-free condition. This seasonal sea ice change is the largest of any of the Arctic or subarctic regions. As expected, the regressed pattern of SIC reveals a strong seasonal

evolution (Fig. 5.5). Negative SIC anomaly persists in the Bering Sea from December to May, while the negative region moves to the Chukchi Sea from June to November.

The superimposed shading in Fig. 5.5 represents the regressed net surface energy flux anomaly. A positive value defines an upward flux from the ocean to the atmosphere. As illustrated in Fig. 5.5, there is a strong spatial coherence between SIC and net surface flux anomalies, although the sign of correlation is reversed between warm (April-August) and cold (November-March) seasons. Negative SIC anomaly generally coincides with negative flux anomaly in the warm season, but with positive flux anomaly in the cold season. The magnitude of the upward flux in the cold season is much larger than the downward flux in the warm season.

In the Arctic and subarctic region including the Bering and Chukchi Seas, two of the most important sea ice related processes that affect air-sea interaction are the ice-albedo feedback and the oceanic heat transport (Screen and Simmonds 2010a, b). Melting sea ice exposes the open water that effectively absorbs incoming sunlight than the sea ice, which leads to an increase in surface air temperature; this so-called ice-albedo feedback can only be active in summer with sufficient insolation (Deser et al 2000). Thus,

the downward heat flux anomaly in the warm season in Fig. 5.5 may be attributed to the increased absorption of solar radiation due to ice-albedo feedback. The flux patterns in the warm season are also consistent with the Arctic Ocean being more efficient in absorbing atmospheric heat during summer (Screen and Simmonds 2010b).

In winter, on the other hand, the primary air-sea interaction mechanism is the oceanic heat transport, since the albedo effect is suppressed due to the low insolation (Screen and Simmonds 2010a, b). Screen and Simmonds (2010b) proposed two explanations for the relationship between SIC and net surface flux in winter season. As a direct response to reductions in winter sea ice cover, heat is released from the relatively warm ocean surface to the colder atmosphere above. As an indirect response, sea ice reduction in summer also facilitates increased heat transfer from the ocean to the atmosphere in winter; sea ice cover reduction in summer leads to heat storage in the ocean, which is released in winter. Indeed, Fig. 5.5 exhibits striking spatial coherence between the negative SIC and the upward flux anomalies in the cold season, which supports that melting sea ice facilitates increased oceanic heat loss. An implication is that sea ice plays a significant role in forcing the atmosphere above by regulating energy flux transfer.

Examining the near-surface air temperature adds further insight into the forcing process from the ocean to the atmosphere. Figure 5.6 shows the regression pattern of 1000-hPa air temperature on the first CSEOF mode of the Bering and Chukchi Seas SSTA in 1999-2010. The largest air temperature anomaly occurs in the winter season, with warming generally coincides with the upward flux anomaly associated with the reduced sea ice cover. Although SSTA warming peaks in summer and the direct ice-albedo feedback is greatest in summer, surface air temperature warming is not so strong in summer (Fig. 5.6). Ocean heat loss in winter is by far a more important source of atmospheric warming. The result presented in this section is consistent with Screen and Simmonds (2010b), who identified the fall-winter energy loss from the Arctic Ocean and the associated air temperature amplification.

CSEOF LVs (Bering/Chukchi, 1999–2010)

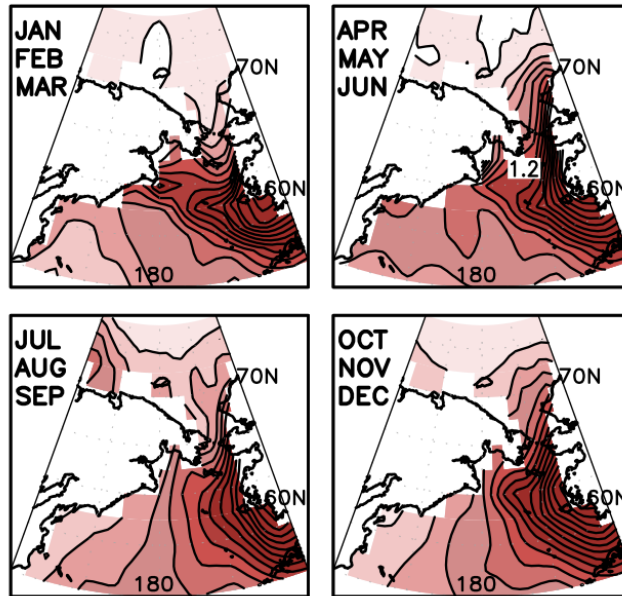


Fig.5.4. Seasonal (3-month) averages of the first CSEOF loading vector of the SSTA in the Bering and Chukchi Seas (160°E-160°W, 54°-76°N) for 1999-2010.

Regressed Field of Net surface Heat Flux (Shading) & Sea Ice Concentration (Contour)

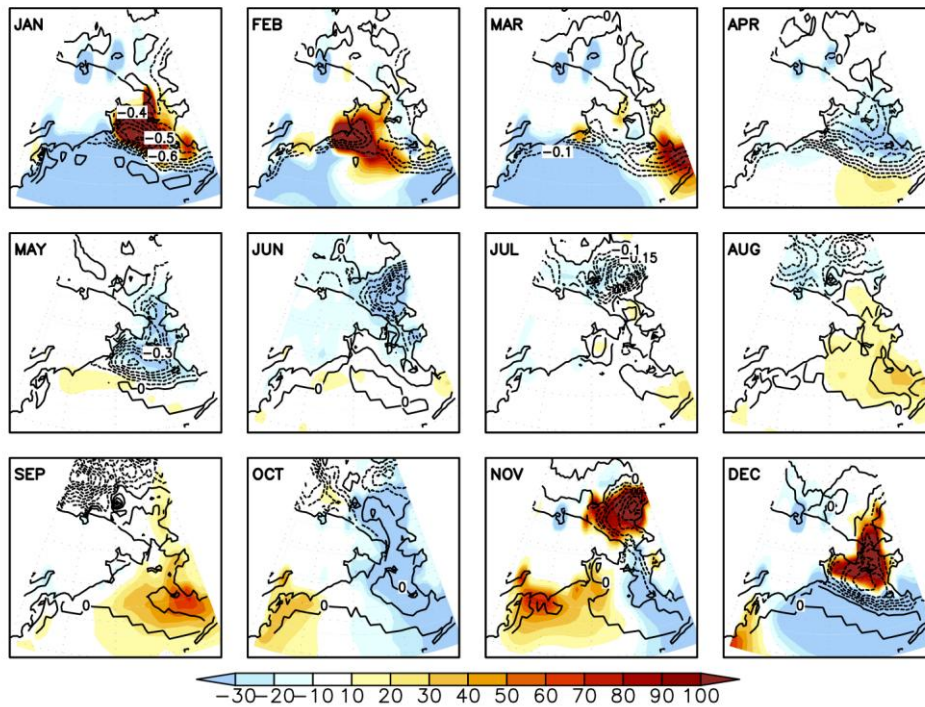


Fig.5.5. The regressed patterns of SIC anomalies (contour) and net surface energy flux anomalies (shading) onto the first CSEOF mode of the Bering and Chukchi Seas SSTA during 1999-2010. The energy flux anomaly is defined as positive in the upward direction.

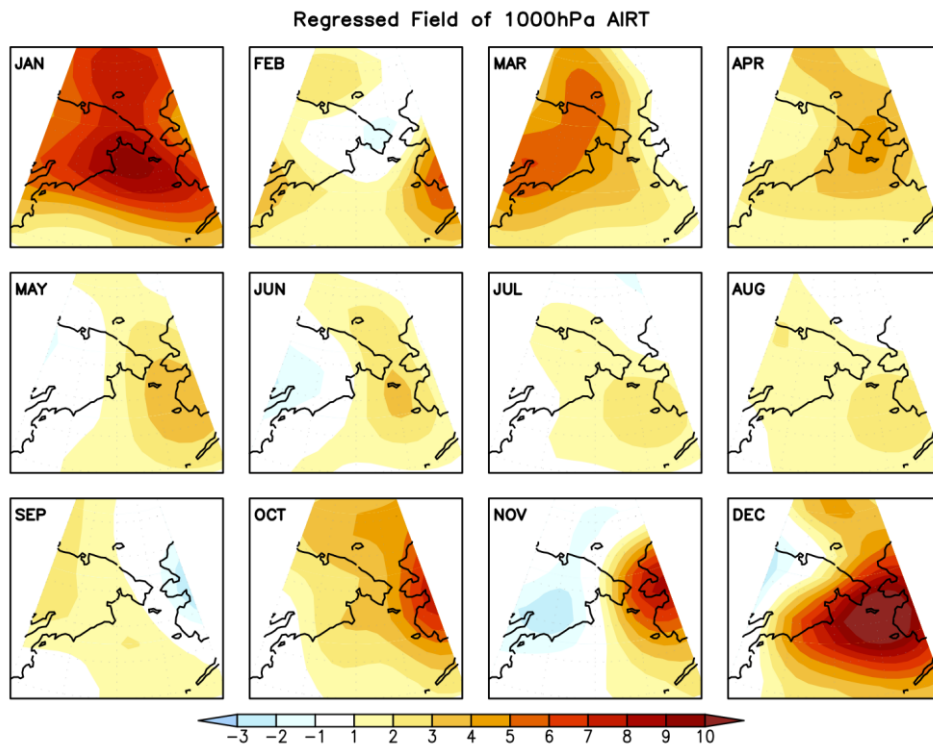


Fig.5.6. The regressed patterns of the 1000-hPa air temperature anomalies onto the first CSEOF mode of the Bering and Chukchi Seas SSTA during 1999-2010.

c. North Pacific atmospheric circulation-regression analysis

Atmospheric response to the recent thermal variability in the Bering Sea does not seem confined to the Bering Sea region, but also appear in the North Pacific. Henceforth, large-scale atmospheric circulation over the North Pacific is investigated in association with the recent thermal state change in the Bering Sea (Fig. 5.4). Figure 5.7 illustrates the regressed 1000-hPa geopotential height (contour), wind (vector), and air temperature (shading) anomalies over the North Pacific region (100°E-80°W, 20°-85°N) onto the leading CSEOF mode of SSTA over the Bering and Chukchi Seas in 1999-2010; the R^2 values are 0.94, 0.95 and 0.92 for geopotential height, wind, and air temperature, respectively. The winter spatial patterns are presented in Fig. 5.7, since upward flux is significant in winter (Fig. 5.5). Although the atmospheric circulation patterns in Fig. 5.7 are comparable to each other, considerable monthly variation is seen in the pattern and amplitude. The 1000-hPa geopotential height in December exhibits negative pressure anomalies over the Bering Sea and the surrounding area (Fig. 5.7a). In January, positive pressure anomalies dominate to the north of 60°N and the negative pressure anomalies shift southward, constituting a north-south dipole structure. This dipole pattern resembles the NPO pattern, which is the second leading mode of North Pacific sea level pressure (Linkin and

Nigam 2008; Rogers 1981). Similar dipole patterns are found in February and March with weaker amplitudes. In particular, a substantial fraction of the Bering Sea region is covered by positive pressure anomalies in January-March.

The accompanying air temperature anomalies, shown as shading in Fig. 5.7, display warm air temperature anomalies to the north of 50°N with centers in the Bering Sea region. The vertical sections of temperature (shading) and geopotential height anomalies (contour) averaged over the Bering Sea region (180°-140°W) are shown in Fig. 5.7. Warming over the Bering Sea is not confined to the lower troposphere but is also evident in the upper troposphere. In December, positive temperature anomalies over the Bering Sea region reach approximately 400 hPa and a baroclinic geopotential height structure with a nodal point near 600 hPa is observed. The linear model result of Hoskins and Karoly (1981) indicates that this baroclinic response is forced by diabatic heating in the lower troposphere associated with surface heat flux deriving from the imposed boundary forcing. In January, on the other hand, an equivalent barotropic structure is observed. The warm air temperature anomaly over the Bering Sea reaches a mature state in January, exhibiting amplification and expansion to near the tropopause. As a result, the thickness of the atmospheric layer increases

further, and the atmospheric circulation adjusts to the equivalent barotropic structure. The adjustment process from an initial baroclinic structure to an equivalent barotropic one was substantiated in atmospheric general circulation models (Peng et al. 2003; Deser et al. 2007). The barotropic dipole structure in January is maintained throughout winter, although the anomaly center varies in location and amplitude. The meridional dipole structure is roughly characterized as an NPO-like pattern. Although the NPO pattern is conventionally known as an intrinsic mode of variability (e.g., Rogers, 1981), an NPO-like pattern seems to appear also as a result of an atmospheric response to the recent thermal forcing in the Bering Sea.

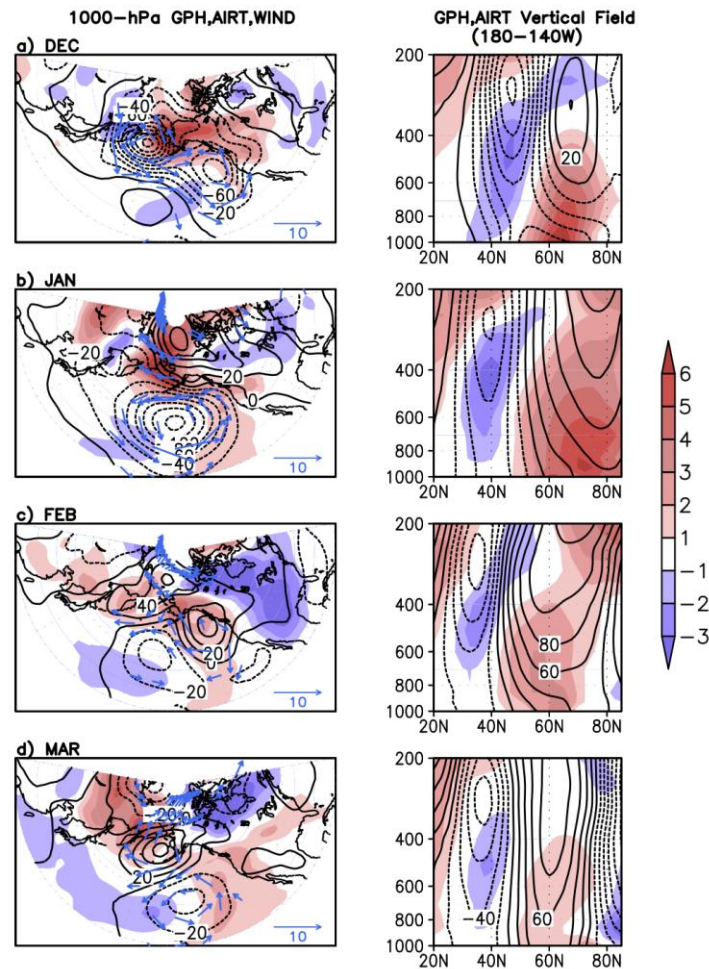


Fig.5.7. The patterns of 1000-hPa geopotential height (contour), wind (vector) and the air temperature (shading) anomalies over the North Pacific (100°E - 80°W , 20° - 85°N) for (a) December, (b) January, (c) February, and (d) March regressed onto the first CSEOF mode of the Bering Sea SSTA for 1999-2010 (left panel), and the vertical sections of the regressed geopotential height (contour), air temperature (shading) anomalies averaged over the longitude band of 180° - 140°W (right panel).

d. North Pacific atmospheric circulation-comparison with the CAM3 model simulation

In order to confirm that the recent thermal condition in the Bering Sea can produce the meridional dipole pattern (i.e., NPO-like response) in winter, two sets of experiments were carried out using the CAM3 model—Clim_Run and SIC_Run. In the Clim_Run experiment, the monthly SST and SIC climatology data from the HadISST dataset for 1980-1998 are used to force CAM3. The SIC_Run experiment is the same as Clim_Run, except over the region of significant sea-ice reduction for 1999-2010; the monthly SST and SIC climatology data for 1999-2010 are used where SIC is reduced by 10% or more compared to 1980-1998. For each set of experiments, the model is integrated for 55 years, and the mean values over the last 50 years are analyzed to exclude the spin-up effect. Assuming that each year is statistically independent, the 50-year mean is equivalent to an ensemble mean of 50 members. The seasonal (3-month) averages of the differences (SIC_Run minus Clim_Run) in the SST (shading) and SIC (contour) boundary conditions are illustrated in Fig. 5.8. SIC has declined more than 10% over the Arctic Ocean in the recent decade (1999-2010) compared to the previous period of 1980-1998. Such a change has already been pointed out in previous studies (Comiso et al. 2008; Maslanik et al. 2007; Stroeve et al.

2007). The Bering and Chukchi Sea ice has also declined except for the summer season (July to September); the sea ice in this region retreats completely in summer. By comparing SIC_Run and Clim_Run experiments, therefore, an atmospheric response to the recent change in the SST and SIC over the Arctic Ocean can be identified. Of particular interest is the atmospheric response over the North Pacific in the winter season. Since the dipole structure is most pronounced in January and February in the regression patterns (Fig. 5.7), analysis for model result will also focus on January and February.

Figure 5.9a shows the difference in the January-February mean of 1000-hPa geopotential height (contour), wind (vector), and air temperature (shading) between the two simulations (SIC_Run minus Clim_Run) over the North Pacific region (100°E - 80°W , 20° - 85°N). The vertical cross-sections of the difference in geopotential height (contour) and air temperature (shading) averaged over the longitude band of 180° - 140°W are illustrated in Fig. 5.9b. The corresponding regression patterns in Fig. 5.7 are reproduced in the lower panel of Fig. 5.9. It is evident that CAM3 captures positive pressure anomaly over the Bering and Chukchi Seas and negative pressure anomaly south of 50°N in response to the warmer SST and reduced SIC. Spatial correlation of the 1000-hPa geopotential height anomaly patterns (Figs. 5.9a

and 5.9c) is 0.75, supporting that the atmospheric response in winter over the North Pacific consists of a meridional dipole structure, which resembles the NPO pattern. In addition, the vertical structure of the response (Fig. 5.9b) exhibits a striking similarity with the regression result (Fig. 5.9d). They share common features of an equivalent barotropic high over 60° - 80° N in association with warming in the entire troposphere and a barotropic low over 30° - 50° N, exhibiting a north-south dipole structure across approximately 50° N. This experimental result supports that the NPO-like atmospheric response may have been derived from the recent warming of the Bering and Chukchi Seas.

CAM3 Model Boundary condition
(SIC_Run–Clim_Run, seasonal mean)

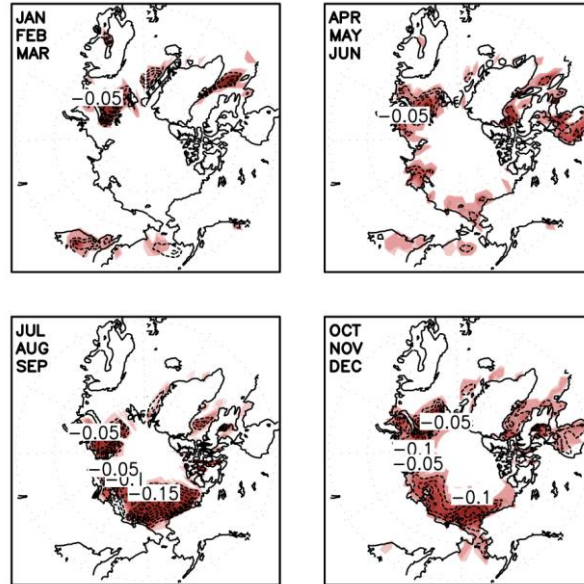


Fig.5.8. The difference (SIC_Run minus Clim_Run) in the SST (shading) and SIC (contour) boundary conditions. Each spatial pattern represents the seasonal (3-month) average of the difference of the boundary conditions.

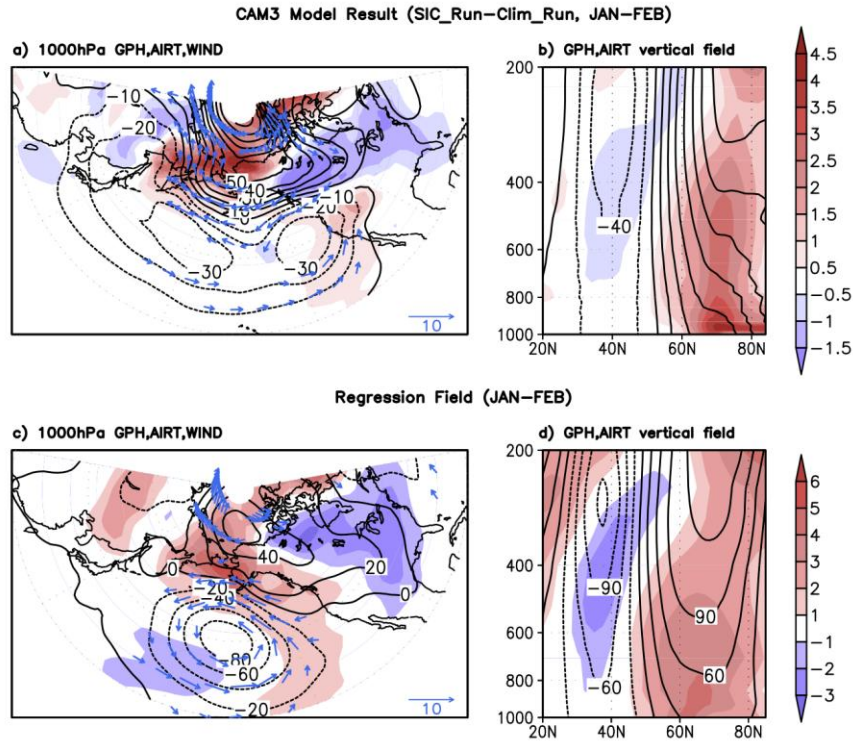


Fig.5.9. (a) The SIC_Run minus Clim_Run difference of the January and February mean 1000-hPa geopotential height (contour), wind (vector) and air temperature (shading) anomalies over the North Pacific (100°E - 80°W , 20° - 85°N) and (b) the difference (SIC_Run minus Clim_Run) of the vertical cross-section of the geopotential height (contour), air temperature (shading) averaged over the longitude band 180° - 140°W . Plotted here are the differences divided by the standard deviation of the first CSEOF PC time series of the Bering Sea SSTA. (c) The January-February mean regressed patterns of 1000-hPa geopotential height, wind and air temperature anomalies and (d) the vertical sections of the geopotential height and air temperature.

5.2. Covariability of Bering Sea and Pacific large-scale circulation

Based on CSEOF analysis and the CAM3 model simulation, it is identified that the warming and sea ice reduction in the Bering and Chukchi Seas during the last decade are closely related to the atmospheric NPO-like pattern. The NPO pattern, a key atmospheric mode in the Pacific basin, is well known for its strong influence on weather patterns over Eurasia and North America, and in particular storm tracks, temperatures, and precipitation (Seager et al. 2005; Linkin and Nigam 2008). The NPO pattern, of course, exerts a strong influence over the Pacific basin; Di Lorenzo et al. (2008) found that the NPO serves as the atmospheric forcing pattern for the oceanic NPGO pattern. Previous studies also emphasized that the regional Bering Sea variability is closely related to the state of the entire Pacific climate system (Niebauer et al. 1988; Minobe 2002).

Figure 5.10 displays the regressed spatial patterns of SSTA and 1000-hPa geopotential height anomalies over the tropical and North Pacific (100°E-80°W, 10°S-70°N). The R^2 values are 0.96 and 0.94 for the SSTA and the geopotential height anomaly, respectively. To further examine the mechanistic details, the regressed patterns of anomalous net surface energy flux and wind at 1000 hPa were also investigated and are shown in Fig. 5.11; the R^2 values are 0.90 and 0.92, respectively. The significant correlations

imply that the recent SST variability in the Bering and Chukchi Seas and the spatial patterns of the Pacific basin depicted in Figs. 5.10 and 5.11 share essentially the same amplitude variation. According to the similarity of the evolution patterns, seasonal mean (3-month) patterns from January to September are presented in Figs. 5.10 and 5.11.

As noted above, the North Pacific atmospheric response to the recent warming in the Bering and Chukchi Seas during winter is the NPO-like pattern (Fig. 5.10a). The corresponding SSTA over the North Pacific bears a strong resemblance to that of the NPGO pattern; the positive SSTA in the eastern North Pacific extends across the Pacific to the western Bering Sea and the Sea of Okhotsk resulting in meridional gradient of SSTA along approximately 40°N. The physical relationship between the NPO and the NPGO SSTA pattern presented in Fig. 5.10a can be explained by the air-sea interaction. As illustrated in Fig. 5.7b, the southerly wind anomaly over the eastern North Pacific advects warm and moist air, leading to warm air temperature anomaly in this region. Note that this warm air temperature anomaly extended southward in the eastern North Pacific does not yet appear in December, since the NPO pattern is not fully established (Fig. 5.7a). The associated net surface flux anomaly in the eastern North Pacific exhibits downward flux (Fig. 5.11a), which subsequently produces a

positive SSTA (Fig. 5.10a). The northerly wind, in contrast, advects cold and dry air into the central North Pacific, resulting in an upward heat flux anomaly and cold SSTA. Although the air-sea interaction appears to be inactive in spring and summer (Figs. 5.11b and c), positive SSTA is observed over the northeastern Pacific for several seasons (Figs. 5.10b and c).

Another important feature in Figs. 5.10 and 5.11 is that the oceanic and atmospheric variations in the North Pacific extend to the subtropical and tropical Pacific. Figure 5.10 displays the positive SSTA extending southwestward from Baja California to the tropical central Pacific. Also, the negative geopotential height extends across much of the Pacific basin from the mid-latitudes to the tropics. This North Pacific-tropical Pacific connection is evident not only in winter but also in spring and summer. The accompanying tropical Pacific SSTA features warming over the tropical central Pacific, that is, CP El Niño (Fig. 5.10). The atmospheric flow over the tropical Pacific displays westerly anomaly extending from the equatorial western to central Pacific and easterly anomaly over the eastern Pacific (Fig. 5.11). Di Lorenzo et al. (2010) suggested that the CP El Niño is tightly linked to the NPGO pattern via atmospheric teleconnection of the NPO. More recent studies have noted that the mid-latitude NPO forcing is particularly influential in the initial establishment of SSTA in the tropical central Pacific

for CP El Niño events (Furtado et al. 2011; Kim et al. 2012; Yu and Kim 2011). This covariability of the NPO, NPGO and CP El Niño is clearly demonstrated in the regression patterns over the Pacific basin in connection with the warming of the Bering and Chukchi Seas during 1999-2010 (Figs. 5.10 and 5.11). Indeed, the CP El Niño events in the recent decade, such as 2002/2003 and 2004/2005, concur with the positive SSTA in the Bering and Chukchi Seas region (see the PC time series in Fig. 5.2). Although data analysis in this study is inconclusive in regard to the cause-effect relationship among the Bering and Chukchi Seas warming, the NPO and the CP El Niño, their physical connectivity has become clearer and stronger during the recent decade.

Regressed SST (shading) & 1000hPa GPH

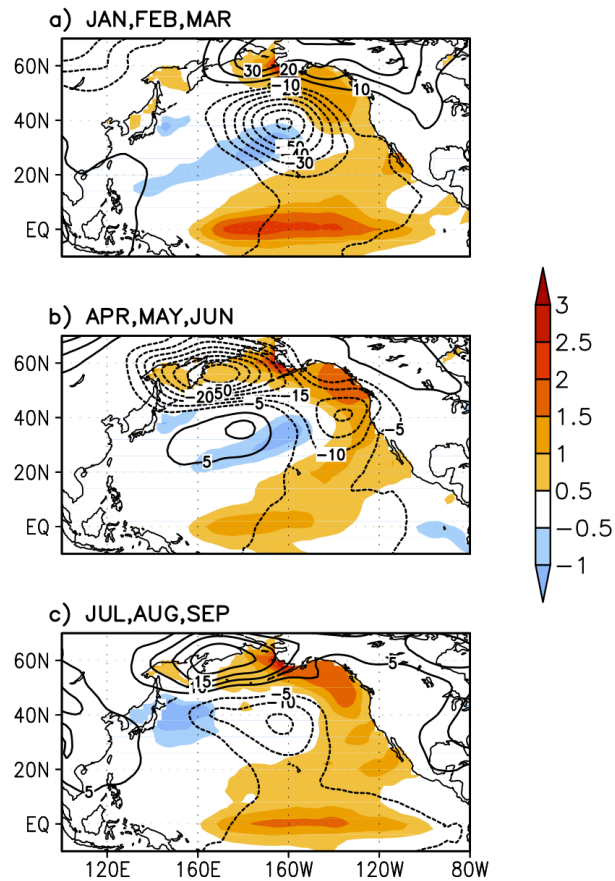


Fig.5.10. The regressed patterns of the 1000-hPa geopotential height anomaly (contour) and SST anomaly (shading) corresponding to the first CSEOF loading vector of the Bering and Chukchi SSTA during the period 1999-2010. Seasonal (3-month) average patterns are represented. Note that contour interval is different for each panel.

Regressed surface heat flux (shading) & 1000hPa Wind

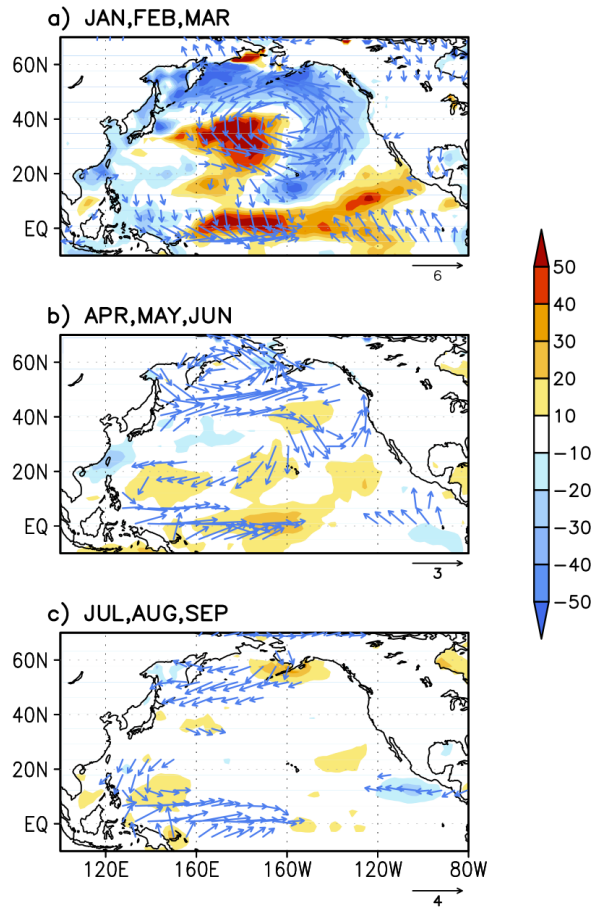


Fig.5.11. The regressed patterns of the 1000-hPa wind anomaly (vector) and net surface energy flux anomaly (shading) corresponding to the first CSEOF loading vector of the Bering and Chukchi SSTA during the period 1999-2010. The seasonal (3-month) average spatial patterns are represented. Note that vector scale is different for each panel.

6. Summary and conclusions

In the present research, a CSEOF analysis was conducted to extract the principal modes of the Pacific climate variability. The third chapter of this thesis presents a refined description of the ENSO characteristics through the three CSEOF modes of SST variability. The first CSEOF mode represents the global warming signal. The loading patterns of the first mode exhibits positive SSTAs over much of the domain and more intense warming is seen in the tropical eastern and central Pacific than in the western Pacific, yielding an appearance of El Niño. In the second CSEOF mode, positive SSTAs in the tropical Pacific are connected with SSTAs of the same sign in the western shore of North America along with negative SSTAs over the western to central North Pacific. The temporal evolution pattern of the second mode indicates that this mode represents low-frequency variability with a strong connection between the North Pacific and the tropical Pacific. The third mode displays biennial oscillation and depicts transitions between El Niño and La Niña over 2-year periods. The third mode fits the canonical picture of ENSO, in which the oscillation mechanism created by tropical Pacific waves dominated. These three principal modes of SST variability are found to be nearly independent of each other. Together, the three modes reproduce the majority of observed SSTAs in the tropical Pacific. In other

words, the bulk of ENSO variability is adequately explained in terms of the interplay among the three modes. The irregular interplay of the three modes has profound implications for physical and dynamical interpretations of ENSO events.

The significant findings in the third chapter are:

- The three dominant modes of the near-global SST variability identified via CSEOF analysis are the global warming mode, the low-frequency variability mode, and the biennial oscillation mode.
- During the strong El Niño events of 1997/98 and 1982/83, all three CSEOF modes contribute positively to these record-breaking El Niño events.
- The CP El Niño events in the early 1990s originated mainly from the low-frequency variability mode, while those in the early 2000s were derived mainly from the global warming mode.

The fourth chapter of this thesis presents that the relationship between the tropical Pacific and the North Pacific has experienced a remarkable change since 1998/99. The extra-tropical atmospheric response to the conventional El Niño primarily drives SST changes over the North Pacific in the period 1980-1998. The SST anomaly and low-level anomalous

atmospheric circulation in the extra-tropics presented for the first period are consistent with the results of previous studies of the “atmospheric bridge mechanism” (Alexander et al. 2002; Deser and Blackmon 1995; Lau and Nath 1996). From 1999 to 2010, however, the ENSO-North Pacific teleconnection displays different characteristic than in the previous period. The most striking feature in the second period is that ENSO-related North Pacific atmospheric variations extend from the mid-latitudes to the subtropical region. Consequently, the mid-latitude atmospheric variability may act as a potential precursor to changes in tropical El Niño characteristics. Note that the tropical SST anomaly patterns in spring and summer are characterized by a CP-type El Niño in the second period. Our results for the second period are consistent with those of previous studies suggesting that mid-latitude atmospheric variability can affect tropical variability (Barnett et al. 1999; Pierce et al. 2000; Vimont et al. 2003a). The present study, however, reveals that the interaction in the opposite direction is also an important link between the tropical Pacific and the North Pacific. Some studies suggested that a frequent occurrence of CP-type El Niño is responsible for the decadal changes in the North Pacific during the recent decades via tropics and mid-latitude atmospheric teleconnection. For example, Di Lorenzo et al. (2010) showed that CP-type El Niño provides a

strong feedback onto the subtropical sea level pressure field in the vicinity of Hawaii, which is close to the southern node of the NPO. In turn, the SLP variation over Hawaii is a major driver of the NPGO, which has been active in the latest decade (Di Lorenzo et al. 2008). In fact, anomalous SST in the central tropical Pacific is most sensitive to SLP variation near Hawaii and may even feedback on the subtropical North Pacific SLP on decadal time scales (e.g., Anderson 2003; Di Lorenzo et al. 2010; Furtado et al. 2012). Therefore, it cannot be ruled out that a frequent occurrence of CP-type El Niño during the recent decade might have resulted in the change in the relationship between the tropical Pacific and the North Pacific.

The principal findings in the fourth chapter are:

- Physical relationship between the dominant SST modes over the tropical Pacific and the North Pacific experienced an abrupt change occurring approximately in late 1990s.
- Atmospheric anomalies induced by the ENSO alter the SST over the North Pacific through surface heat flux change during the period of 1980-1998.
- During the period of 1999-2010, in contrast, the mid-latitude atmospheric variability may act as a potential precursor to change in tropical El Niño characteristics.

The fifth chapter of this thesis presents a plausible cause of recent climate transition in association with the global warming signal. Warming in the Bering Sea in the second period is closely associated with major atmospheric variability in the North Pacific. Specifically, CSEOF analysis reveals that the recent warming and resultant reduction in SIC in the Bering Sea induce an NPO-like atmospheric response; an experiment with the CAM3 model confirms and supports this connection between the Bering Sea and the North Pacific. Since the NPO pattern is characterized by a southward shift in the atmospheric action center, it exerts substantial influence on the subtropical and tropical Pacific. Furthermore, several recent studies argued that the initial establishment of SST anomalies in the tropical central Pacific is intimately tied to mid-latitude atmospheric variability, that is, the NPO pattern (Furtado et al. 2011; Kim et al. 2012; Yu and Kim 2011). Indeed, the CP El Niño appears as the regression pattern of the tropical Pacific SSTA onto the first CSEOF mode of the Bering Sea SSTA for 1999-2010. In summary, present study suggests that the NPO-like pattern could be induced by the recent changes in thermal state of the Bering and Chukchi Seas, and this NPO-like structure is closely tied to the tropical CP El Niño variations.

The significant findings in the fifth chapter are:

- After the unusual thermal condition of the Bering Sea in 1997/98, it is found that the recent climate variability (1999-2010) in the Bering Sea is closely related to Pacific basin-scale atmospheric and oceanic circulation patterns.
- The atmospheric response to the recent warming in the Bering Sea resembles the NPO pattern
- Recent climate variability in the Bering Sea has strong covariability with large-scale climate modes in the Pacific, that is NPGO and CP El Niño.

Reference

- Alexander, M. A. (1990), Simulation of the response of the North Pacific Ocean to the anomalous atmospheric circulation associated with El Niño, *Clim. Dyn.*, 5, 53-65.
- Alexander, M. A. (1992a), Midlatitude atmosphere–ocean interaction during El Niño. Part I: The North Pacific Ocean, *J. Clim.*, 5, 944–958.
- Alexander, M. A. (1992b), Midlatitude atmosphere–ocean interaction during El Niño. Part II: the Northern Hemisphere atmosphere, *J. Clim.*, 5, 959–972.
- Alexander, M. A., I. Bladé, M. Newman, J. R. Lanzante, N. C. Lau, and J. D. Scott (2002), The atmospheric bridge: The influence of ENSO teleconnections on air-sea interaction over the global oceans, *J. Clim.*, 15(16), 2205-2232.
- Anderson, B. (2003), Tropical Pacific sea-surface temperatures and preceding sea level pressure anomalies in the subtropical North Pacific, *J. Geophys. Res.*, 108, 4732
- Ashok, K., S. K. Behera, S. A. Rao, H. Weng, and T. Yamagata (2007), El Niño Modoki and its possible teleconnection, *J. Geophys. Res.*, 112, C11007.
- Barnett, T. (1991), The interaction of multiple time scales in the tropical climate system, *J. Clim.*, 4(3), 269-285.
- Barnett, T. P., D. W. Pierce, M. Latif, D. Dommenges, and R. Saravanan (1999), Interdecadal interactions between the tropics and midlatitudes in the Pacific basin, *Geophys. Res. Lett.*, 26(5), 615-618.
- Battisti, D. S., and A. C. Hirst (1989), Interannual variability in a tropical atmosphere–ocean model: Influence of the basic state, ocean geometry, and nonlinearity, *J. Atmos. Sci.*, 46, 1687-1712.
- Bjerknes, J. (1966), A possible response of the atmospheric Hadley circulation to equatorial anomalies of ocean temperature, *Tellus*, 18(4), 820-829.
- Bjerknes, J. (1969), Atmospheric teleconnections from the equatorial Pacific 1, *Mon. Weath. Rev.*, 97(3), 163-172.
- Boer, G., B. Yu, S.-J. Kim, and G. Flato (2004), Is there observational support for an El Niño-like pattern of future global warming?, *Geophys. Res. Lett.*, 31(6), L06201.

- Bond, N. A., J. E. Overland, M. Spillane, and P. Stabeno (2003), Recent shifts in the state of the North Pacific, *Geophys. Res. Lett.*, *30*(23), 2183.
- Brodeur, R. D., C. E. Mills, J. E. Overland, G. E. Walters, and J. D. Schumacher (1999), Evidence for a substantial increase in gelatinous zooplankton in the Bering Sea, with possible links to climate change, *Fish. Oceanogr.*, *8*(4), 296-306.
- Cai, W., and P. H. Whetton (2000), Evidence for a time-varying pattern of greenhouse warming in the Pacific Ocean, *Geophys. Res. Lett.*, *27*(16), 2577-2580.
- Ceballos, L. I., Di Lorenzo, C. D. Hoyos, N. Schneider, and B. Taguchi (2009), North Pacific Gyre Oscillation synchronizes climate fluctuations in the eastern and western boundary systems, *J. Clim.*, *22*(19), 5163-5174.
- Collins, M. (2005), El Niño-or La Niña-like climate change?, *Clim. Dyn.*, *24*(1), 89-104.
- Collins, W. D., P. J. Rasch, B. A. Boville, J. J. Hack, J. R. McCaa, D. L. Williamson, B. P. Briegleb, C. M. Bitz, S. J. Lin, and M. Zhang (2006), The formulation and atmospheric simulation of the Community Atmosphere Model version 3 (CAM3), *J. Clim.*, *19*(11), 2144-2161.
- Comiso, J. C., C. L. Parkinson, R. Gersten, and L. Stock (2008), Accelerated decline in the Arctic sea ice cover, *Geophys. Res. Lett.*, *35*, L01703.
- Compo, G. P., et al., (2011), The twentieth Century Reanalysis Project. *Q. J. Geol. Meteorol. Soc.*, *137*, 1-28.
- Deser, C., and M. L. Blackmon (1995), On the relationship between tropical and North Pacific sea surface temperature variations, *J. Clim.*, *8*(6), 1677-1680.
- Deser, C., J. E. Walsh, and M. S. Timlin (2000), Arctic sea ice variability in the context of recent atmospheric circulation trends, *J. Clim.*, *13* (3), 617-633.
- Deser, C., R. A. Tomas, and S. Peng (2007), The transient atmospheric circulation response to North Atlantic SST and sea ice anomalies, *J. Clim.*, *20*, 4751-4767.
- Deser, C., R. Tomas, M. Alexander, and D. Lawrence (2010), The seasonal atmospheric response to projected Arctic sea ice loss in the late twenty-first century, *J. Clim.*, *23*(2), 333-351.

- Di Lorenzo, E., N. Schneider, K. M. Cobb, P. J. S. Franks, K. Chhak, A. J. Miller, J. C. McWilliams, S. J. Bograd, H. Arango, E. Curchister, T. M. Powell, and P. Rivere (2008), North Pacific Gyre Oscillation links ocean climate and ecosystem change, *Geophys. Res. Lett.*, *35*, L08607.
- Di Lorenzo, E., K. M. Cobb, J. C. Furtado, N. Schneider, B. T. Anderson, A. Bracco, M. A. Alexander, and D. J. Vimont (2010), Central Pacific El Niño and decadal climated change in the North Pacific, *Nature Geoscience*, *3*, 762-765.
- Furtado, J. C., E. Di Lorenzo, B. T. Anderson, and N. Schneider (2011), Linkages between the North Pacific Oscillation and central tropical Pacific SSTs at low frequencies, *Clim. Dyn.*, doi: 10.1007/s00382-011-1245-4.
- Goddard, L., and N. E. Graham (1997), El Nino in the 1990s, *J. Geophys. Res.*, *102*(C5), 10423-10410,10436.
- Graham, N. (1994), Decadal-scale climate variability in the tropical and North Pacific during the 1970s and 1980s: Observations and model results, *Clim. Dyn.*, *10*(3), 135-162.
- Grebmeier, J. M., J. E. Overland, S. E. Moore, E. V. Farley, E. C. Carmack, L. W. Cooper, K. E. Frey, J. H. Helle, F. A. McLaughlin, and S. L. McNutt (2006), A major ecosystem shift in the northern Bering Sea, *Science*, *311*(5766), 1461-1464.
- Gu, D., and S. G. Philander (1997), Interdecadal climate fluctuations that depend on exchanges between the tropics and extratropics, *Science*, *275*(5301), 805-807.
- Hare, S. R., and N. J. Mantua (2000), Empirical evidence for North Pacific regime shifts in 1977 and 1989, *Prog. Oceanogr.*, *47*(2-4), 103-145.
- Horel, J. D., and J. M. Wallace (1981), Planetary-scale atmospheric phenomena associated with the Southern Oscillation, *Mon. Weath. Rev.*, *109*, 813-829.
- Hoskins, B. J., and D. J. Karoly (1981), The steady linear response of a spherical atmosphere to thermal and orographic forcing, *J. Atmos. Sci.*, *38*(6), 1179-1196.
- Hunt Jr, G. L., C. Baduini, R. Brodeur, K. Coyle, N. Kachel, J. Napp, S. Salo, J. Schumacher, P. Stabeno, and D. Stockwell (1999), The Bering Sea in

- 1998: the second consecutive year of extreme weather-forced anomalies, *Eos Trans. AGU*, 80(47), 561-566.
- Hunt Jr, G. L., P. Stabeno, G. Walters, E. Sinclair, R. D. Brodeur, J. M. Napp, and N. A. Bond (2002), Climate change and control of the southeastern Bering Sea pelagic ecosystem, *Deep Sea Res., Part II*, 49(26), 5821-5853.
- Ji, M., A. Leetmaa, and V. E. Kousky (1996), Coupled model predictions of ENSO during the 1980s and the 1990s at the National Centers for Environmental Prediction, *J. Clim.*, 9(12), 3105-3120.
- Jin, F.-F. (1997a), An equatorial ocean recharge paradigm for ENSO. Part I: Conceptual model, *J. Atmos. Sci.*, 54(7), 811-829.
- Jin, F.-F. (1997b), An equatorial ocean recharge paradigm for ENSO. Part II: A stripped-down coupled model, *J. Atmos. Sci.*, 54(7), 830-847.
- Kanamitsu, M., W. Ebisuzaki, J. Woollen, S. K. Yang, J. Hnilo, M. Fiorino, and G. Potter (2002), Ncep-doe amip-ii reanalysis (r-2), *Bull. Am. Meteorol. Soc.*, 83(11), 1631-1644.
- Kao, H. Y., and J. Y. Yu (2009), Contrasting eastern-Pacific and central-Pacific types of ENSO, *J. Clim.*, 22, 615-632.
- Kaplan, A., M. A. Cane, Y. Kushnir, A. C. Clement, M. B. Blumenthal, B. Rajagopalan (1998), Analyses of global sea surface temperature 1854–1991, *J. Geophys. Res.*, 103(18), 567–589.
- Kim, H., P. Webster, J. Curry (2009), Impact of shifting patterns of Pacific Ocean warming on north Atlantic tropical cyclones, *Science* 325, 77–80.
- Kim, K.-Y. (2002), Investigation of ENSO variability using cyclostationary EOFs of observational data, *Meteor. Atmos. Physics*, 81(3), 149-168.
- Kim, K.-Y., Y.-Y. Kim (2002), Mechanism of Kelvin and Rossby waves during ENSO events, *Meteor. Atmos. Physics*, 81(3), 169–189
- Kim, K. Y., and G. R. North (1997), EOFs of harmonizable cyclostationary processes, *J. Atmos. Sci.*, 54(19), 2416-2427.
- Kim, K. Y., and J. W. Roh (2010), Physical Mechanisms of the Wintertime Surface Air Temperature Variability in South Korea and the near-7-Day Oscillations, *J. Clim.*, 23(8), 2197-2212.
- Kim, K. Y., G. R. North, and J. Huang (1996), EOFs of one-dimensional cyclostationary time series: Computations, examples, and stochastic modeling, *J. Atmos. Sci.*, 53(7), 1007-1007.

- Kim, K. Y., R. J. Park, K. R. Kim, and H. Na (2010), Weekend effect: Anthropogenic or natural, *Geophys. Res. Lett.*, *37*, L09808.
- Kim, S. T., J.-Y. Yu, Kumar, A., and Wang, H. (2012), Examination of the two types of ENSO in the NCEP CFS Model and its extratropical associations, *Mon. Weath. Rev.*, *140*, 1908-1923, doi : 10.1175/MWR-D-11-00300.1.
- Kim, W., S.-W. Yeh, J.-H. Kim, J.-S. Kug, and M. Kwon (2011), The unique 2009–2010 El Niño event: A fast phase transition of warm pool El Niño to La Niña, *Geophys. Res. Lett.*, *38*(15), L15809.
- Kleeman, R., R. Colman, N. Smith, and S. Power (1996), A recent change in the mean state of the Pacific Ocean: Observational evidence, atmospheric response and implications for coupled modeling, *J. Geophys. Res.*, *101*(20), 483-420.
- Kleeman, R., J. McCreary, and B. Klinger (1999), A mechanism for generating ENSO decadal variability, *Geophys. Res. Lett.*, *26*(12), 1743-1746.
- Kruse, G. H. (1998), Salmon run failures in 1997-1998: A link to anomalous ocean conditions?, *Alaska Fish. Res. Bull.*, *5*(1), 55-63.
- Kug, J.-S., and I.-S. Kang (2006), Interactive feedback between ENSO and the Indian Ocean, *J. Clim.*, *19*(9), 1784-1801.
- Kug, J. S., F. F. Jin, and S. I. An (2009), Two types of El Niño events: cold tongue El Niño and warm pool El Niño, *J. Clim.*, *22*, 1499-1515.
- Larkin, N. K., and D. Harrison (2005), Global seasonal temperature and precipitation anomalies during El Niño autumn and winter, *Geophys. Res. Lett.*, *32*, L16705.
- Latif, M., and T. P. Barnett (1996), Decadal climate variability over the North Pacific and North America: Dynamics and predictability, *J. Clim.*, *9*, 2407-2423.
- Latif, M., R. Kleeman, and C. Eckert (1997), Greenhouse warming, decadal variability, or El Nino? An attempt to understand the anomalous 1990s, *J. Clim.*, *10*(9), 2221-2239.
- Lau, N. C., and M. J. Nath (1996), The role of the " atmospheric bridge" in linking tropical Pacific ENSO events to extratropical SST anomalies, *J. Clim.*, *9*(9), 2036-2057.

- Lau, N. C., and M. J. Nath (2001), Impact of ENSO on SST variability in the North Pacific and North Atlantic: Seasonal dependence and role of extratropical sea-air coupling, *J. Clim.*, 14(13), 2846-2866.
- Lee, T., and M. J. McPhaden (2010), Increasing intensity of El Niño in the central-equatorial Pacific, *Geophys. Res. Lett.*, 37(14), L14603.
- Lim, Y. K., and K. Y. Kim (2007), ENSO impact on the space-time evolution of the regional Asian summer monsoons, *J. Clim.*, 20(11), 2397-2415.
- Linkin, M. E., and S. Nigam (2008), The north pacific oscillation-west Pacific teleconnection pattern: Mature-phase structure and winter impacts, *J. Clim.*, 21(9), 1979-1997.
- Mantua, N. J., and S. R. Hare (2002), The Pacific decadal oscillation, *J. Oceanogr.*, 58(1), 35-44.
- Mantua, N. J., S. R. Hare, Y. Zhang, J. M. Wallace, and R. C. Francis (1997), A Pacific interdecadal climate oscillation with impacts on salmon production, *Bull. Am. Meteorol. Soc.*, 78(6), 1069-1080.
- Maslanik, J., C. Fowler, J. Stroeve, S. Drobot, J. Zwally, D. Yi, and W. Emery (2007), A younger, thinner Arctic ice cover: Increased potential for rapid, extensive sea-ice loss, *Geophys. Res. Lett.*, 34 (24), L24501.
- Meehl, G. A., and W. M. Washington (1996), El Niño-like climate change in a model with increased atmospheric CO₂ concentrations, *Nature*, 382(6586), 56-60.
- Miller, A. J., D. R. Cayan, T. P. Barnett, N. E. Graham, and J. M. Oberhuber (1994), The 1976–77 climate shift of the Pacific Ocean, *Oceanography*, 7(1), 21-26.
- Minobe, S. (2000), Spatio-temporal structure of the pentadecadal variability over the North Pacific, *Prog. Oceanogr.*, 47(2), 381-408.
- Minobe, S. (2002), Interannual to interdecadal changes in the Bering Sea and concurrent 1998/99 changes over the North Pacific, *Prog. Oceanogr.*, 55(1-2), 45-64.
- National Research Council (1996), The Bering Sea ecosystem, *National Academy Press*, Washington, DC.
- Napp, J. M., and G. L. Hunt Jr (2001), Anomalous conditions in the south-eastern Bering Sea 1997: linkages among climate, weather, ocean, and Biology, *Fish. Oceanogr.*, 10 (1), 61-68.

- Niebauer, H. (1988), Effects of El Niño–Southern Oscillation and North Pacific weather patterns on interannual variability in the subarctic Bering Sea, *J. Geophys. Res.*, 93 (C5), 5051-5068.
- Neelin, J. D., D. S. Battisti, A. C. Hirst, F.-F. Jin, Y. Wakata, T. Yamagata, and S. E. Zebiak (1998), ENSO theory, *J. Geophys. Res.*, 103(C7), 14261-14214.
- Overland, J. E., J. M. Adams, and N. A. Bond (1999), Decadal variability of the Aleutian Low and its relation to high-latitude circulation, *J. Clim.*, 12(5), 1542-1548.
- Overland, J. E., and P. J. Stabeno (2004), Is the climate of the Bering Sea warming and affecting the ecosystem, *Eos Trans. AGU*, 85(33), 309-316.
- Pan, Y., and A. H. Oort (1990), Correlation analyses between sea surface temperature anomalies in the eastern equatorial Pacific and the world ocean, *Clim. Dyn.*, 4(3), 191-205.
- Peng, S., W. A. Robinson, and S. Li (2003), Mechanisms for the NAO responses to the North Atlantic SST tripole, *J. Clim.*, 16 (12), 1987-2004.
- Peterson, W. T., and F. B. Schwing (2003), A new climate regime in northeast Pacific ecosystems, *Geophys. Res. Lett.*, 30(17), 1896.
- Pierce, D. W., T. P. Barnett, and M. Latif (2000), Connections between the Pacific Ocean tropics and midlatitudes on decadal timescales, *J. Clim.*, 13(6), 1173-1194.
- Rayner, N., D. Parker, E. Horton, C. Folland, L. Alexander, D. Rowell, E. Kent, and A. Kaplan (2003), Global analyses of sea surface temperature, sea ice, and night marine air temperature since the late nineteenth century, *J. Geophys. Res.*, 108(D14), 4407.
- Rasmusson, E. M., and T. H. Carpenter (1982) Variations in tropical sea surface temperature and surface wind fields associated with the Southern Oscillation/El Niño, *Mon. Wea. Rev.*, 110 (5), 354–384
- Rasmusson, E. M., X. Wang, and C. F. Ropelewski (1990), The biennial component of ENSO variability, *Journal of Marine Systems*, 1(1), 71-96.
- Rogers, J. C. (1981), The North Pacific Oscillation, *J. Climatol.*, 1, 39-57.
- Schumacher, J., N. Bond, R. Brodeur, P. Livingston, J. Napp, and P. Stabeno (2003), Climate change in the southeastern Bering Sea and some consequences for biota, *Large Marine Ecosystems of the World: Trends in Exploitation, Protection, and Research*, 17-40.

- Schwing, F., and C. Moore (2000), A year without summer for California, or a harbinger of a climate shift?, *EOS Transactions*, *81*, 301-305.
- Screen, J. A., and I. Simmonds (2010a), The central role of diminishing sea ice in recent Arctic temperature amplification, *Nature*, *464*(7293), 1334-1337.
- Screen, J. A., and I. Simmonds (2010b), Increasing fall-winter energy loss from the Arctic Ocean and its role in Arctic temperature amplification, *Geophys. Res. Lett.*, *37*(16), L16707.
- Seo, K. H., and K. Y. Kim (2003), Propagation and initiation mechanisms of the Madden-Julian oscillation, *J. Geophys. Res.*, *108*(4384), 10.1029.
- Seager, R., N. Harnik, W. Robinson, Y. Kushnir, M. Ting, H. P. Huang, and J. Velez (2005), Mechanisms of ENSO-forcing of hemispherically symmetric precipitation variability, *Q. J. Roy. Meteor. Soc.*, *131*(608), 1501-1527.
- Suarez, M. J., and P. S. Schopf (1988), A delayed action oscillator for ENSO, *J. Atmos. Sci.*, *45*(21), 3283-3287.
- Simmons, A., J. Wallace, and G. Branstator (1983), Barotropic wave propagation and instability, and atmospheric teleconnection patterns, *J. Atmos. Sci.*, *40*, 1363-1392.
- Smith, T. M., R. W. Reynolds, T. C. Peterson, and J. Lawrimore (2008), Improvements to NOAA's historical merged land-ocean surface temperature analysis (1880-2006), *J. Clim.*, *21*(10), 2283-2296.
- Stabeno, P., N. Bond, and S. Salo (2007), On the recent warming of the southeastern Bering Sea shelf, *Deep Sea Res., Part II*, *54*(23-26), 2599-2618.
- Stabeno, P., N. Bond, N. Kachel, S. Salo, and J. Schumacher (2001), On the temporal variability of the physical environment over the south-eastern Bering Sea, *Fish. Oceanogr.*, *10*(1), 81-98.
- Stockwell, D. A., T. E. Whitledge, S. I. Zeeman, K. O. Coyle, J. M. Napp, R. D. Brodeur, A. I. Pinchuk, and G. L. Hunt Jr (2001), Anomalous conditions in the south-eastern Bering Sea, 1997: nutrients, phytoplankton and zooplankton, *Fish. Oceanogr.*, *10*(1), 99-116.
- Stroeve, J., M. M. Holland, W. Meier, T. Scambos, and M. Serreze (2007), Arctic sea ice decline: Faster than forecast, *Geophys. Res. Lett.*, *34*, L09501.

- Tanimoto, Y., K. Hanawa, Y. Toba, and N. Iwasaka (1993), Characteristic variations of sea surface temperature with multiple time scales in the North Pacific, *J. Clim.*, 6(6).
- Timmermann, A., J. Oberhumber, A. Bacher, M. Esch, M. Latif and E. Roeckner (1999), Increased El Niño frequency in a climate model forced by future greenhouse warming, *Nature*, 398, 694-697
- Trenberth, K. E. (1990), Recent observed interdecadal climate changes in the Northern Hemisphere, *Bull. Am. Meteorol. Soc.*, 71(7), 988-993.
- Trenberth, K. E., and J. W. Hurrell (1994), Decadal atmosphere-ocean variations in the Pacific, *Clim. Dyn.*, 9(6), 303-319.
- Vimont, D. J., D. S. Battisti, and A. C. Hirst (2001), Footprinting: A seasonal connection between the tropics and mid-latitudes, *Geophys. Res. Lett.*, 28(20), 3923-3926.
- Vimont, D. J., D. S. Battisti, and A. C. Hirst (2003a), The Seasonal Footprinting Mechanism in the CSIRO General Circulation Models, *J. Clim.*, 16(16), 2653-2667.
- Vimont, D. J., J. M. Wallace, and D. S. Battisti (2003b), The Seasonal Footprinting Mechanism in the Pacific: Implications for ENSO, *J. Clim.*, 16, 2668-2675.
- Wallace, J. M., and D. S. Gutzler (1981), Teleconnections in the geopotential height field during the Northern Hemisphere winter, *Mon. Weath. Rev.*, 109, 784- 812.
- Xie, S.-P., and S. G. H. Philander (1994), A coupled ocean-atmosphere model of relevance to the ITCZ in the eastern Pacific. *Tellus*, 46A, 340-350.
- Yeh, S. W., J. S. Kug, B. Dewitte, M. H. Kwon, B. P. Kirtman, and F. F. Jin (2009), El Niño in a changing climate, *Nature*, 461(7263), 511-514.
- Yeh, S. W., Y. J. Kang, Y. Noh, and A. J. Miller (2011), The North Pacific climate transitions of the winters of 1976/77 and 1988/89, *J. Clim.*, 24, 1170-1183.
- Yeo, S.-R., K.-Y. Kim, S.-W. Yeh, W. Kim (2012), Decadal changes in the relationship between the tropical Pacific and the North Pacific, *J. Geophys. Res.*, 117 (D15), D15102.

- Yoo, S. H., J. Fasullo, S. Yang, C. H. Ho (2010) On the relationship between Indian Ocean sea surface temperature and the transition from El Niño to La Niña. *J. Geophys. Res.*, 115, D15114.
- Yu, J.-Y., H.-Y. Kao, and T. Lee (2010), Subtropics-related interannual sea surface temperature variability in the equatorial central Pacific, *J. Clim.*, 23, 2869-2884.
- Yu, J.-Y., and Kim, S. T. (2011), Relationship between extratropical sea level pressure variations and central Pacific and eastern Pacific types of ENSO, *J. Clim.*, 24, 708-720.
- Zhang, Y., J. M. Wallace, and N. Iwasaka (1996), Is climate variability over the North Pacific a linear response to ENSO?, *J. Clim.*, 9(7), 1468-1478.

국문 초록

태평양 기후의 온난화, 장 주기, 2 년 주기 변동 성분과 1990 년대 후반에 나타난 10 년 변화의 특징

여새림

지구환경과학부

서울대학교 대학원

다양한 물리적 기작이 혼재되어 있는 태평양의 기후변동성을 이해하기 위하여 주기적 정상 경험 직교 함수 (CSEOF) 통계 분석 방법을 도입하여 태평양 기후 변동성을 물리적으로 독립적인 주요 모드로 나누어 살펴보았다.

1871 년부터 2010 년까지 전 지구 해수면 온도의 CSEOF 분석 결과 온난화 신호, 장 주기 변동성, 그리고 2 년 주기 변동 성분의 세 가지 주요 모드가 추출되었다. 이 세 가지 모드의 합은 관측된 엘니뇨-남방진동 (ENSO)의 주요 변동성을 나타낸다. 즉, 열대 태평양의 ENSO 변동성은 세 가지 모드의 상호작용으로 설명될 수 있다. 구체적으로 1982/83 이나 1997/98 에 나타난 매우 강한 규모의 엘니뇨의 경우 세 가지 모드의 양의 아노말리가 함께 영향을 미친 결과이다. 또한 새로운 타입의 엘니뇨인 중태평양 엘니뇨의 경우 1990 년대와 2000 년대의 물리적 기작이 서로 다르게 나타났다. 즉, 1990 년대의 중태평양 엘니뇨의 경우에는 장 주기 변동성분이 큰 영향을

미친 반면, 2000 년대의 중태평양 엘리뇨의 경우에는 온난화 신호가 큰 영향을 미쳤다는 것을 확인하였다.

한편, 태평양 기후의 장 주기 변동성분에 따르면 가장 최근의 장 주기 전이는 1998/99 년을 기준으로 음의 상태에서 양의 상태로 전이되었다. 이와 함께 1998/99 년 이전과 이후에 열대태평양과 북태평양의 관련성이 크게 변화한 것을 확인 할 수 있는데, 각 기간의 열대 태평양과 북태평양의 물리적 관련성의 특징에 대하여 조사하였다. 1980 년부터 1998 년 기간에는 열대 태평양의 ENSO 로부터 유도되는 북태평양 대기 변동성이 대기-해양간 열속 교환을 통하여 북태평양 기후 변동성에 큰 영향을 미치는 과정이 주요하게 작용하였다. 한편 1999 년부터 2010 년 기간에는 ENSO 와 관련한 북태평양의 대기 변동성이 평균적인 대기 변동성의 위치보다 남하해서 나타나는 North Pacific oscillation(NPO) 대기 패턴의 특징을 보인다. 이러한 북태평양의 대기 변동성은 아열대 지역 및 열대지역으로까지 대기-해양 상호작용을 통하여 영향을 미칠 수 있다. 특히 열대 태평양으로의 중위도 대기 변동성의 영향은 최근에 발생 빈도가 높아진 중태평양 엘리뇨와 관련되어 있다는 것을 확인하였다.

1999 년을 기준으로 장 주기 변동성의 상 변화뿐만 아니라 온난화 신호의 강화도 매우 뚜렷하게 나타났다. 이러한 온난화 신호가 최근 태평양 기후 변동성에 어떠한 영향을 미쳤는지 조사하였다. 특히 해빙의 존재로 온난화 신호가 강화되어 나타날 수 있는 해역인 베링해와 척치해 지역에서의 온난화 신호를 추출하고 이것이 최근 태평양 기후 변동성에 어떠한 영향을 미쳤는지 확인하였다. 구체적으로 1999 년부터 2010 년 기간의 베링해 지역의 온난화로 인한 해빙의 감소는 해양에서 대기로의

열속의 방출을 유도하여 북태평양 대기 변동성에 영향을 미친다. 관련된 북태평양 대기 변동성은 NPO 대기 패턴으로써, 북태평양과 열대태평양의 대기-해양 변동성을 연결시켜 주는 역할을 한다. 실제로 베링해 지역의 최근 변동성과 관련한 열대 태평양의 기후 변동성은 중태평양 엘리뇨로써, 최근 태평양의 주된 기후 변동성과 베링해 지역의 온난화 신호가 밀접하게 관련되어 있다는 것을 확인하였다.

주요어: 엘리뇨-남방진동, 온난화, 주기적 정상 경험 직교함수
학번 : 2009-20372